Generalized Cyclic Plasticity Constitutive Model for Sands within a Hyperplasticity Framework

Olgu Orakci[1,2], George Anoyatis[2], Shiao Huey Chow[1], and Stijn François[3]

[1]Department of Infrastructure Engineering, The University of Melbourne, Victoria 3010, Australia
[2]Department of Civil Engineering, KU Leuven Campus Bruges, Bruges 8200, Belgium
[3]Department of Civil Engineering, KU Leuven Campus Arenberg, Leuven 3001, Belgium

Abstract

This study presents a novel generalized cyclic plasticity model within the hyperplasticity framework for modeling the cyclic behavior of sands. The formulation adopts a multisurface plasticity approach that accommodates multiple yield criteria, namely Tresca, von Mises, Drucker–Prager, Mohr–Coulomb , Matsuoka–Nakai, and Lade–Duncan. Following the generalized principle of maximum dissipation, the proposed Generalized Cyclic Plasticity (GCP) model introduces a third potential into Ziegler's classical two-potential thermodynamics framework, enabling a rigorous treatment of non-associative plasticity. The framework further incorporates critical state soil mechanics (CSSM) through a state-parameter-linked dilatancy angle and employs a phase transformation condition that governs the transition between contraction and dilation. This combination reproduces the monotonic and cyclic response of loose and dense states. The model parameters are physically interpretable and can be calibrated using standard soil laboratory tests. These features allow the GCP model to reproduce a wide spectrum of behaviors, including excess pore pressure generation, cyclic mobility, stiffness and damping evolution with cycling, Lode angle dependency, shakedown through pressure-dependent combined hardening, and dilation and contraction responses within the CSSM framework. The numerical implementation is based on robust return mapping algorithms that avoid numerical instabilities near the apex of the yield surface. The modular structure of the formulation enables exact recovery of classical constitutive models such as associative and non-associative Mohr–Coulomb and Prevost, while systematically extending them through optional features including enhanced dilatancy and hardening laws, thereby providing a unified framework for benchmarking and model development. The model performance is evaluated through triaxial and direct simple shear tests.

1 Introduction

Soil behavior under cyclic loading is complex and strongly nonlinear, leading to nonlinear stiffness degradation, hysteresis upon unloading and reloading, and progressive accumulation of volumetric and shear strains. These mechanisms are particularly crucial in offshore geotechnical applications for foundations in sandy soils supporting wind turbines, where long-term cyclic loading can induce irreversible deformations, alter stiffness and damping, and generate excess pore water pressures [43, 54, 16, 29]. Such responses are governed by "soil memory", where the soil material response depends on the current stress state as well as its loading history [43].

Classical constitutive models, such as the commonly adopted Mohr–Coulomb (MC) or hardening plasticity alternatives, provide useful approximations for engineering applications but are limited in their ability to accurately reproduce cyclic sand behavior. In particular, the MC model employs a fixed yield surface together with an elastic perfectly plastic response, which prevents it from capturing cyclic accumulation (ratcheting), stiffness degradation, cyclic mobility, and liquefaction. Hardening models fall short in capturing evolving fabric or reverse-loading effects, often generating path-independent responses, unrealistic shakedown, or unbounded ratcheting. Such limitations have prompted the development of models that explicitly incorporate memory effects, dilatancy evolution, and history-dependent stiffness.

Corresponding author Stijn François. stijn.francois@kuleuven.be

A wide range of approaches has been proposed to introduce fabric dependence and loading history into constitutive models. These approaches include scalar variables such as the overconsolidation ratio [47], interpolation-based approaches including the High Cycle Accumulation (HCA) model [39], ratcheting-integrated macro-elements [16], memory-enhanced p–y curves [25], and constitutive models employing memory surfaces such as the Prevost model [42], the Hujeux model [20, 38], SANISAND–MS [29] and SANISAND–MSf [56], and HySand [46]. While each approach offers distinct advantages, they also pose challenges related to underlying model assumptions, calibration requirements, and numerical robustness.

The seminal work by Prevost (1985) [42], captures essential features of cyclic mobility, including pore pressure generation and plastic strain accumulation under cyclic loading. It accounts for changes in shear strength and damping characteristics. However, the dilatancy mechanism is introduced via a phase transformation line, and does not account for the critical state [6]. Consequently, a single parameter set cannot be applied across different soil states. In addition, its original yield function may become unstable at low confining pressures, particularly near the apex of the yield surface, and the Mroz translation rule [37] requires continuous detection of the active surface, which may lead to response discontinuities [6].

Since the development of the Prevost model, various formulations have been developed to integrate both critical state behavior and the phase transformation line, enabling the representation of state-dependent dilation and contraction in sands. The state parameter [3] is widely adopted in critical state soil mechanics (CSSM) based soil constitutive models, as it provides a robust framework for representing sand behavior across different densities and stress levels, capturing both contractive and dilative trends within a single parameter set [31, 29, 48, 46]. This concept underpins advanced constitutive models such as NorSand [23] and the SANISAND family [31, 9, 29, 56].

NorSand (1993) [23] is a critical state-based elasto-plastic model developed to capture sand behavior across a wide range of densities and confining pressures. It uses the state parameter to capture density and stress dependency effects and employs a single bullet-shaped yield surface with an internal cap and a non-associative flow rule. This framework enables realistic modeling of liquefaction triggering and prediction of post-liquefaction strength while maintaining relatively straightforward implementation. However, NorSand does not explicitly account for memory or bounding surfaces, which naturally limits its ability to capture cyclic effects such as stiffness degradation and dilatancy under complex loading paths.

The SANISAND family evolved incrementally from the development of the landmark CSSM-based framework by Manzari and Dafalias (1997) [31], combining the state parameter with bounding surface plasticity to capture density effects, fabric evolution, and cyclic response. The models employ a phase transformation and a hardening surface that evolve with the state parameter. The formulation postulates the direction of plastic strain increments rather than deriving it from a plastic potential. This approach reproduces the dilatancy and cyclic response trends observed in experiments for the targeted simulations. However, this assumption can also lead to nonphysical effects such as overshooting [12]. SANISAND–MS [29], an extension of SANISAND04 [9], introduces a memory surface to improve ratcheting and load reversal behavior, but does not capture cyclic mobility. SANISAND–MSf [56] was later developed to address this limitation and reproduce cyclic mobility under undrained conditions, including butterfly-shaped stress paths. Despite these advances, parameter calibration remains nontrivial due to pronounced density-dependent behavior [51], and numerous studies report that identifying a single parameter set capable of reproducing both monotonic and cyclic responses is exceedingly difficult [51, 12]. Furthermore, limitations persist in representing pore pressure evolution under long-term cyclic loading, highlighting the need for continued refinement of memory-enhanced bounding surface formulations.

HySand [46] is built on the previous works of Houlsby and coworkers [15, 17, 19] and is formulated within a thermodynamically consistent hyperplasticity framework and explicitly accounts for state-dependent behavior. Unlike classical plasticity formulations where the direction of the plastic flow is obtained by differentiating a plastic potential with respect to stress, the critical state framework is incorporated through pertinent kinematic constraints enforced by Lagrange multipliers on the yield function, following the methodology reported in previous works of Houlsby [15, 17]. This approach requires plastic evolution to be expressed as the gradient of a differentiable potential, rather than merely enforcing positive dissipation, which is a more restrictive condition than the classical Clausius–Planck inequality [7]. While

this ensures thermodynamic consistency, it introduces physical complexities, as contraction and dilation are governed by separate mechanisms, and dilation evolves with plastic strains through anisotropy. These features can hinder straightforward calibration of model parameters. The formulation has also been reported to show numerical instability at low pressures, which can be mitigated in practice by applying a small surcharge [44].

The Hujeux model [20, 38] is a multi-mechanism elastoplastic formulation developed to simulate cyclic and monotonic behavior of granular soils. It combines isotropic and deviatoric hardening with a non-associated flow rule based on dilatancy principles, allowing smooth transitions between contractive and dilative states. This structure enables the model to reproduce characteristic cyclic features such as hysteresis, strain accumulation, and volumetric changes. However, it involves a large number of parameters that require complex calibration, while its performance may degrade under highly irregular or long-duration cyclic loading due to reliance on predefined plastic mechanisms.

In light of the above and with a view toward realistic long-term analyses, there remains a need for a constitutive model capable of capturing the full load-response while maintaining reliability under the inherent complexity of cyclic conditions [16]. Although existing models provide valuable insights, few can accurately capture long-term cyclic accumulation of sands [1], and it remains challenging for a single, physically interpretable parameter set to capture cyclic mobility, ratcheting, and critical state behavior across varying stress levels, soil densities, and loading modes. In addition, robust constitutive models require adherence to thermodynamic principles [13, 19, 50], ensuring a physically admissible dissipation mechanism and a well-posed evolution of the internal variables under cyclic loading [50]. Taken together, these considerations motivate the development of a constitutive framework that balances physical realism, mathematical tractability, and practical applicability.

To achieve this objective, this study proposes a framework drawing on concepts from multisurface plasticity with kinematic hardening, which provides a natural foundation for modeling cyclic soil response. Such models can reproduce key features of the cyclic behavior, including the Bauschinger effect and Masing behavior [16, 14], hysteresis [42], and shear-induced anisotropy [43]. The framework, adopting discretized plastic moduli, allows representation of softening, hardening, and ratcheting [6], while back-stress tensors encode loading history and memory [19, 6]. In addition, incorporating isotropic hardening enables shakedown-type responses under long-term cyclic loading [29, 50]. Further, the kinematic hardening formulation is extended to account for the soil state and cyclic degradation. Taken together, these hardening mechanisms can be formulated to incorporate pressure dependence and constitute the conceptual foundation of the proposed GCP model.

Capturing these desired features, the present work develops the Generalized Cyclic Plasticity (GCP) model, a multisurface plasticity formulation that is thermodynamically consistent and designed to reproduce hysteretic cyclic behavior, satisfy the original Masing rule, and capture the contractive and dilative responses of sands under complex stress paths associated with cyclic loading. Rooted in the principles of hyperplasticity, the proposed model derives its incremental stress–strain response from three potentials: (i) free energy Ψ, characterizing elastic and plastic contributions; (ii) yield function f, defining the onset of plasticity; and (iii) plastic flow potential g, governing strain evolution via dilation parameter, in line with the generalized principle of maximum dissipation [50]. The use of potentials provides a unified and physically grounded formulation that avoids ad hoc flow rules while retaining the flexibility required to capture characteristic cyclic mechanisms observed in sands [17]. The dilation parameter is linked to the state parameter following Jefferies [24], providing a realistic representation of the volumetric strain evolution with density and pressure, and is combined with a state dependent phase transformation criterion. To further enhance the predictive capabilities, the proposed model accounts for realistic strength asymmetry between triaxial compression and extension, a feature observed in sands due to particle contact orientation, and is herein governed by the Lode angle [30]. This is achieved by employing multiple yield surface definitions, following the work by Lagioia and Panteghini [27], including Matsuoka–Nakai [33], Lade–Duncan [26], von Mises [34], Drucker–Prager [11], Tresca [49], and Mohr–Coulomb [8, 35] with optional rounded forms. Within the GCP framework, the general yield surface enables the model to capture the Lode-angle dependence of yield and strength, while the same functional form is employed

to construct the plastic potential, thereby preserving thermodynamic consistency through a variational structure consistent with the generalized principle of maximum dissipation.

The novelty of the GCP model lies in its ability to capture the complex dilative behavior of sands using an single set of physically interpretable soil parameters, which can be obtained from standard laboratory element tests. This parameter set is sufficient to simulate both monotonic and cyclic soil responses, under undrained conditions across a wide range of applied pressures and soil material densities. Derived within a thermodynamically consistent hyperplasticity framework, the formulation provides a unified and physically grounded structure that avoids ad hoc flow rules while ensuring admissible dissipation and a well-posed evolution of the internal variables. To the authors' knowledge, existing state-dependent sand models do not explicitly link the state-controlled peak dilation angle to the phase transformation condition within the flow potential; instead, the proposed formulation introduces a simple and transparent coupling that preserves smoothness while reproducing observed contractive–dilative transitions. The formulation incorporates dedicated numerical strategies for stable integration, including a linearized yield-surface representation, analytical Jacobians, and a return-mapping algorithm designed to improve convergence near the yield-surface apex. Particular attention is given to non-associative Matsuoka–Nakai and Lade–Duncan flow potentials, for which a dedicated stabilization strategy is developed to address numerical challenges arising from dilation-angle dependence. An additional feature of the formulation is its configurability: GCP can reproduce established models, including associative or non-associative Mohr–Coulomb or the Prevost model [42], providing natural baselines for validation. Beyond replication, the framework allows extension of these classical models by activating features introduced in this study, such as Lode-angle dependency, non-associative integration of critical state soil mechanics, stiffness degradation, and pressure and void ratio dependent combined hardening, thereby offering a versatile model for simulating sand behavior across a broad range of loading scenarios.

The structure of the paper is organized as follows. Section 2 introduces the constitutive formulation, including the general yield-surface concept, pressure-dependent elastic moduli, non-associative plastic flow, and multisurface plasticity with combined hardening. The section also details the three scalar potentials used to define the elastic response, plastic flow, and hardening evolution, as well as the incorporation of critical state concepts through the state parameter and dilation angle. Section 3 presents the numerical implementation, including the implicit return-mapping algorithm, consistency condition for multisurface plasticity, and the methodology for simulating triaxial and direct simple shear tests. Section 4 verifies the model through triaxial test simulations benchmarked against the Prevost model [6]. Section 5 demonstrates the capabilities and versatility of the model, highlighting key insights from the simulations. Finally, Section 6 summarizes the study and presents the main findings. This work focuses on establishing the conceptual basis of the GCP model and presenting its mathematical formulation in a systematic manner. The emphasis is placed on describing the underlying principles, defining the model equations, and verifying the formulation against reference simulations reported in the literature. Detailed calibration of model parameters against laboratory test data for specific sands, as well as applications involving finite element analyses with large loading cycles in boundary-value problems, are beyond the scope of the present paper and are considered topics for future work.

2 Development of the proposed GCP model

This section outlines the formulation of the proposed Generalized Cyclic Plasticity (GCP) model. The general yield surface, pressure-dependent elastic moduli, and non-associative flow rule are first introduced. The multisurface plasticity framework with combined isotropic and kinematic hardening is then established, followed by the hyperplasticity potentials and the enforcement of thermodynamic consistency. Finally, critical state concepts are embedded in the model.

2.1 General yield surface

A tension-positive sign convention is adopted in view of its numerical implementation, employing the Cauchy stress and strain tensors throughout. The principal stresses, defined as the eigenvalues of the stress tensor $\boldsymbol{\sigma}$, are ordered as $\sigma_3 \leq \sigma_2 \leq \sigma_1$, each acting normally on a plane where the shear stress vanishes. The prime symbol $'$ is omitted throughout the text since all stresses mentioned are effective stresses. The stress tensor is decomposed into hydrostatic and deviatoric components as:

$$\boldsymbol{\sigma} = p\,\mathbf{I} + \boldsymbol{\sigma}_{\mathrm{dev}} \tag{1}$$

where $p = \frac{1}{3}\,\mathrm{tr}(\boldsymbol{\sigma})$ denotes the mean effective stress, tr is the trace operator, $\mathbf{I}$ is the second-order identity tensor, and $\boldsymbol{\sigma}_{\mathrm{dev}}$ is the deviatoric stress tensor. The deviatoric invariants of $\boldsymbol{\sigma}$ are denoted by $J_{1\boldsymbol{\sigma}}$, $J_{2\boldsymbol{\sigma}}$, and $J_{3\boldsymbol{\sigma}}$, such that:

$$J_{1\boldsymbol{\sigma}} = \mathrm{tr}(\boldsymbol{\sigma}_{\mathrm{dev}}) = 0, \qquad J_{2\boldsymbol{\sigma}} = \frac{1}{2}\,\|\boldsymbol{\sigma}_{\mathrm{dev}}\|^2 \quad \text{where } \|\square\| = \sqrt{\sum_i \sum_j (\square)_{ij}^2}, \qquad J_{3\boldsymbol{\sigma}} = \det(\boldsymbol{\sigma}_{\mathrm{dev}}) \tag{2}$$

In compact tensor notation, the dot $(\cdot)$ denotes single contraction, while the colon $(:)$ indicates double contraction. The notation $\|\bullet\|_{\square} := \sqrt{\bullet : \square : \bullet}$ is adopted for a second-order tensor $\bullet$, where $\square$ denotes a fourth-order tensor that induces a weighted Euclidean norm.

Classical models such as Drucker–Prager [11], which do not incorporate the effect of the intermediate principal stress σ_2, exhibit a circular cross-section around the hydrostatic axis (see Figure 1a) and therefore predict identical compression and extension stress ratios ($M_{\mathrm{c}} = M_{\mathrm{e}}$). In contrast, more advanced criteria such as Matsuoka–Nakai [33] and Lade–Duncan [26] include the influence of the intermediate stress and introduce Lode-angle dependence, enabling differentiation between M_{c} and M_{e}, thus improving predictive capability under complex loading paths. In this regard, the Lode angle [30] characterizes the influence of the third deviatoric stress invariant $J_{3\boldsymbol{\sigma}}$ on material behavior under different principal stress states. For the domain $-\pi/6 \leq \theta \leq \pi/6$, it is defined as:

$$\theta = \frac{1}{3}\,\arcsin\left(\frac{\sqrt{27}}{2}\,\frac{J_{3\boldsymbol{\sigma}}}{J_{2\boldsymbol{\sigma}}^{3/2}}\right) \tag{3}$$

With reference to the Matsuoka–Nakai (MN) yield surface [33], the convex reformulation introduced by Panteghini and Lagioia [40] provides an equivalent expression that removes the non-convex branches of the original formulation and retains only the physically admissible compression surface. Noting that this convexified expression shares the same mathematical structure as other classical failure criteria, Lagioia and Panteghini [27] demonstrated that the original and rounded Tresca [49], von Mises [34], Drucker–Prager [11], classical and rounded Mohr–Coulomb [8, 35] by inner and outer tangent approximations, and Lade–Duncan [26] criteria can all be expressed within a general formulation by using shape parameters α, β, and γ, listed in Table 1. The resulting general yield surface provides a smooth approximation with at least C^2 continuity across all six Mohr–Coulomb and Tresca surfaces [27]. Figure 1(a) illustrates the resulting limit stress conditions for $\varphi = 35°$, $c = 0$, and $\beta = 0.95$ (i.e., the rounding parameter [27] for the rounded Tresca and rounded Mohr–Coulomb both by inner and outer tangent approximations).

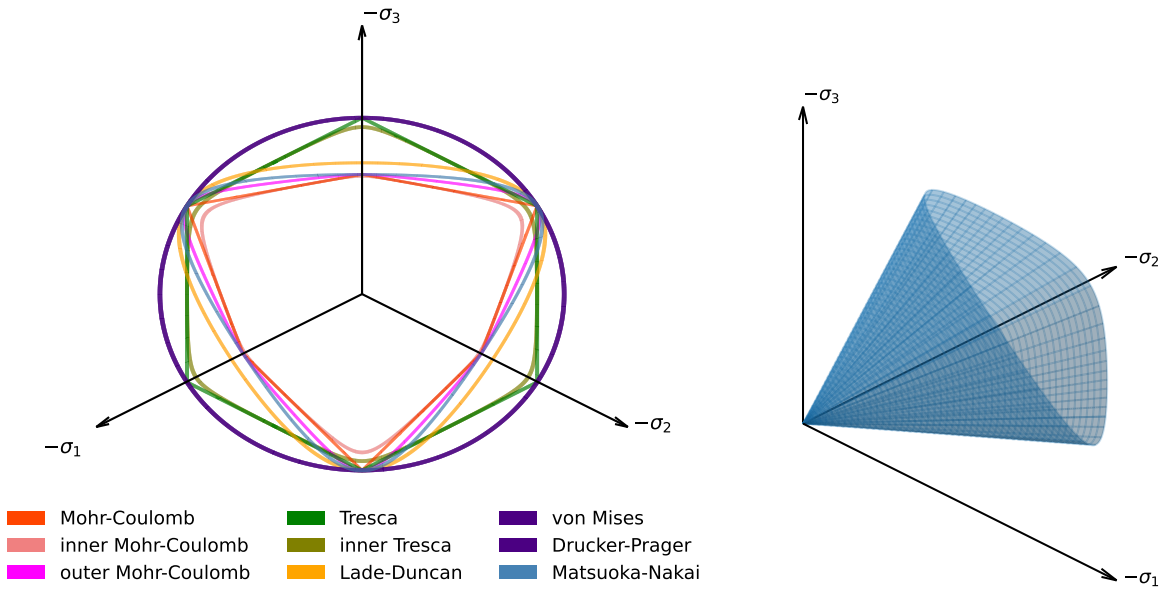

(a) (b)

Figure 1: Yield surfaces of the general failure criteria (a) all yield surfaces and (b) Matsuoka–Nakai yield surface. Surfaces are set to have the same strength for triaxial compression conditions $\theta = -\pi/6$.

Table 1: Shape function parameters α, β, and γ for the general yield surface following the original work by Lagioia and Panteghini [27]

yield criteria	α	β	γ
von Mises and Drucker–Prager	1	0	1
Tresca	$\sec\left[\frac{\pi}{6}\right]$	1	1
rounded Tresca	$\sec\left[\frac{\pi}{6}\right]$	< 1	1
Mohr–Coulomb	$\sec\left[(\bar{\gamma}+1)\frac{\pi}{6}\right]$	1	$1-\bar{\gamma}$
inner Mohr–Coulomb	$\sec\left[(\bar{\gamma}+1)\frac{\pi}{6}\right]$	< 1	$1-\bar{\gamma}$
outer Mohr–Coulomb	$\csc\left[(1+\gamma)\frac{\pi}{6}+\frac{\arccos\beta}{3}\right]$	< 1	$\frac{2}{\pi}\left[-3\arctan\left(\frac{\sin\varphi\cot\frac{\arcsin\beta}{3}}{3+\sin\varphi}\right)-3\tan\frac{\arcsin\beta}{3+\sin\varphi}+\arccos\beta\right]$
Matsuoka–Nakai	$2\sqrt{A_1}A_\varphi$	$\frac{A_2}{A_1^{3/2}}$	0
Lade–Duncan	$2\sqrt{A_1}A_\varphi$	$\frac{A_2}{A_1^{3/2}}$	0

where $\bar{\gamma} = \frac{6}{\pi}\arctan\left(\frac{\sin\varphi}{\sqrt{3}}\right)$. A_1 and A_2 are given in Eq. (12) and Eq. (13) for Matsuoka–Nakai and Lade–Duncan criteria, respectively.

The general yield surface [27] is expressed as a function of the mean effective stress p, the square root of the second deviatoric stress invariant $J = \sqrt{J_{2\boldsymbol{\sigma}}}$, and the Lode angle θ:

$$f(p, J, \theta) \;=\; -C \;+\; A_\varphi\, p \;+\; J\,\Gamma(\theta) \;=\; 0 \tag{4}$$

where

$$\Gamma(\theta) = \alpha\cos\left[\frac{\arccos\left(\beta\sin 3\theta\right)}{3} - \gamma\,\frac{\pi}{6}\right] \tag{5}$$

$A_\varphi = \frac{M}{\sqrt{3}}$ where M is the slope of the meridional section in triaxial compression at the critical state. Because the Lode angle in Eq. (4) automatically distinguishes between compression and extension, it is sufficient to define M only for triaxial compression. The parameter A_φ is chosen so that all deviatoric surfaces exhibit the same strength in triaxial compression ($\theta = -\pi/6$), leading to:

$$A_\varphi = \frac{2\sqrt{3}\,\sin\varphi}{3-\sin\varphi} \tag{6}$$

The general yield surface provides the foundation of the GCP model, allowing different yield surface formulations to be specified within the unified expression in Eq. (4).

2.2 Definition of pressure-dependent elastic moduli

In many geomaterials, particularly cohesionless soils, elastic moduli depend on the mean effective stress, reflecting the nonlinear elastic response commonly observed in these materials. In this work, the elastic law adopts a Janbu-type stress dependency [22], with shear and bulk moduli varying as a power of the mean effective stress. Although the shear modulus is known to vary also with void ratio and and this dependence is incorporated in some sand models [9], the present study adopts the simpler stress-dependent expression employed by Prevost [42], omitting void-ratio dependence to maintain focus on model verification, such that:

$$\mu = \mu_{\text{ref}} \left(\frac{p}{p_{\text{ref}}} \right)^{\beta} \qquad K = K_{\text{ref}} \left(\frac{p}{p_{\text{ref}}} \right)^{\beta} \tag{7}$$

where μ and K denote the shear and bulk moduli, respectively; μ_{ref} and K_{ref} are the corresponding moduli at the reference mean effective stress p_{ref}, and β is an experimentally determined pressure-sensitivity index.

2.3 Implementation of non-associativity

The general form of the yield criteria introduced in Eq. (4) is employed to construct the plastic potential function, enabling the recovery of a variational structure and the associated convex duality within a non-associative framework. In line with the generalized principle of maximum dissipation [50], the proposed GCP model extends Ziegler's thermodynamic framework through the introduction of a third independent potential, thereby establishing a thermodynamically consistent variational treatment of non-associative material behavior. In particular, the model employs:

i. the free energy Ψ, characterizing elastic and plastic contributions (detailed in Section 2.4.1);

ii. the yield function f, defining the onset of plastic deformation;

iii. the plastic flow potential g, governing the direction of plastic strain evolution.

The plastic flow potential adopts herein the same functional form as the yield surface defined in Eq. (4), excluding the cohesion term. Following the usual treatment of non-associated plasticity in soil constitutive modeling, the plastic potential is obtained by replacing the friction angle φ with the dilation angle ψ. Accordingly, the dilation parameter A_ψ replaces A_φ, and is given by:

$$A_\psi = \frac{2\sqrt{3}\,\sin\psi}{3 - \sin\psi} \tag{8}$$

The function $\Gamma(\theta)$ in Eq. (5) remains unchanged for the Tresca, von Mises, and Drucker–Prager criteria. For the Matsuoka–Nakai, Lade–Duncan, and Mohr–Coulomb criteria, it is replaced by its dilation counterpart $\hat{\Gamma}(\theta)$, since the corresponding shape parameters depend on the dilation angle ψ (see Table 1). This substitution preserves the functional form of the yield function f and plastic potential g while introducing non-associativity [50]. Accordingly, the general form can be defined as:

$$g(p, J, \theta) \;=\; A_\psi\, p \;+\; J\,\hat{\Gamma}(\theta) \tag{9}$$

The direction of plastic flow in stress space, $\boldsymbol{m}$, is obtained from the subdifferential of the plastic potential with respect to the stress tensor

$$\boldsymbol{m} = \frac{\partial g}{\partial \boldsymbol{\sigma}} \tag{10}$$

which, in the adopted Cauchy stress representation, is expressed in Voigt notation as a 6×1 vector.

Numerical Stabilization for Matsuoka–Nakai (MN) and Lade–Duncan (LD) Potentials
Direct application of this form to the MN and LD criteria leads to non-convergence in implicit integration schemes because the gradient vanishes when $\psi = 0$ ($A_\psi = 0$), and reverses direction for $\psi < 0$. This behavior arises from the original formulation of the MN and LD yield surfaces, in which both the pressure and shear terms are scaled by A_φ to fit the general yield structure [27]. Employing this original form in the flow potential yields:

$$g(\sigma) = \sqrt{3}\, A_\psi\, p + 2\, J \sqrt{A_1}\, A_\psi \cos\left[\frac{\arccos\left(\dfrac{A_2}{A_1^{3/2}}\, \sin 3\theta\right)}{3}\right] \tag{11}$$

where A_1 and A_2 depend on material strength K_{MN} and K_{LD} through:

$$A_1 = \frac{K_{\mathrm{MN}} - 3}{K_{\mathrm{MN}} - 9}, \qquad A_2 = \frac{K_{\mathrm{MN}}}{K_{\mathrm{MN}} - 9} \qquad \text{where} \quad K_{\mathrm{MN}} = \frac{9 - \sin^2\psi}{1 - \sin^2\psi} \tag{12}$$

$$A_1 = \frac{K_{\mathrm{LD}}}{K_{\mathrm{LD}} - 27}, \qquad A_2 = A_1 \qquad \text{where} \quad K_{\mathrm{LD}} = \frac{(3 - \sin\psi)^3}{(1 + \sin\psi)(1 - \sin\psi)^2} \tag{13}$$

To improve the numerical stability of the plastic flow direction in Eq. (10), we remove the A_ψ-dependent multiplier from g, resulting in the final form of the plastic potential:

$$g(\sigma) \;=\; p \;+\; J\,\frac{2}{\sqrt{3}}\,\sqrt{A_1}\,\cos\left[\frac{\arccos\left(\dfrac{A_2}{A_1^{3/2}}\,\sin 3\theta\right)}{3}\right] \tag{14}$$

This modification affects both the volumetric and deviatoric components of $\boldsymbol{m}$. The volumetric part is no longer given by $\frac{A_\psi}{3}\,\mathbf{I}$, but instead becomes $\boldsymbol{m}_{\mathrm{v}} = \frac{\mathbf{I}}{3}$. The deviatoric component, governed by the shape parameter α (see Table 1), likewise becomes independent of A_ψ. As a result, the full gradient $\boldsymbol{m}$ no longer depends on A_ψ.

However, the resulting $\boldsymbol{m}_{\mathrm{v}}$ is identical for positive and negative ψ. To distinguish between dilation and contraction, we reintroduce the influence of ψ solely through a sign factor $A_\psi \,/\, |A_\psi|$ applied to $\boldsymbol{m}_{\mathrm{v}}$. This adjustment preserves the sign of the dilation angle while maintaining numerical robustness. This approach is consistent with hyperplastic and variational interpretations of non-associativity [50], as well as with the common practice of treating volumetric dilatancy separately from the deviatoric flow direction. To the authors' knowledge, this two-step stabilization for MN/LD potentials has not been previously reported.

2.4 Multisurface plasticity with combined isotropic and kinematic hardening

This study adopts the nested yield surface concept originally introduced by Mroz [37], which provides high flexibility for capturing complex soil material behavior observed in experiments. The approach enables accurate calibration by assigning distinct stiffness and strength parameters to each surface [18]. A schematic representation of the model with N yield surfaces and the corresponding load-displacement response are shown in Figures 2a and 2b, respectively. The evolution of these surfaces during triaxial cyclic loading is illustrated in Figure 3 in two- and three-dimensional stress spaces. In Figure 3a, all yield surfaces are initially homothetic and nested. During isotropic consolidation, the stress point remains on the hydrostatic axis, indicating that no shear is mobilized (Figure 3a). At this stage, the response is purely elastic and governed by the bulk and shear moduli, K and μ, respectively, which are represented by a single linear spring as shown in Figure 2a. When the sample is sheared under triaxial loading, the stress point

departs from the hydrostatic axis and approaches the innermost yield surface while the response remains elastic. Upon reaching this surface (surface 1 in Figure 2a), it is activated (Figure 3b), and plastic strain begins to develop. At this stage, the load-deformation response incorporates the hardening contribution of the surface, as illustrated by the red curve associated with hardening modulus H_1 in Figure 2b, leading to an increase in the overall stiffness of the system. The loading direction $\boldsymbol{n}$ (Eq. (25)) is shown in Figures 3b and 3c. Owing to the non-associative nature of the formulation, the plastic strain naturally evolves along a different direction, $\boldsymbol{m}$ (Eq. (10)). Additional shearing causes the activated surface to translate and/or expand according to the hardening rule, eventually contacting the next surfaces i.e., surfaces 2, 3, ..., N^{th}, and dragging them along with the evolving stress state as loading progresses. Each additional surface is subsequently activated upon contact, and ultimately all active surfaces translate collectively. This produces the characteristic hardening and the associated increase in stiffness observed in the load-displacement response, as shown in Figure 2b.

Upon unloading, the response is initially elastic and then transitions to plastic as the stress point contacts the innermost surface in the unloading direction and drags it along. As unloading proceeds, additional nested surfaces are activated sequentially. These surfaces translate and/or expand in the direction of unloading (blue arrow on Figure 3c). Each newly activated surface contributes incrementally to the total plastic strain and the stiffness, enabling the model to capture the accumulation of cyclic plasticity and the associated hardening or softening behavior. The plastic flow directions of all active surfaces are determined independently according to their respective plastic potentials, while the total stress increment is obtained from the contributions from each surface, consistent with the multisurface framework. This behavior is consistent with experimental observations on silica sand [52]. Figure 2b demonstrates compliance with the original Masing rule over a complete loading-unloading-reloading cycle.

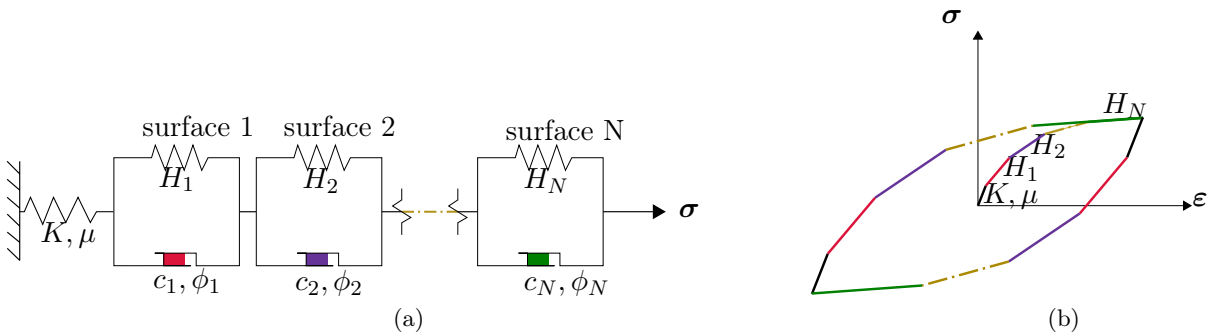

Figure 2: Conceptual representation of nested yield surfaces: (a) schematic representation of the multi-surfaces and (b) corresponding load-displacement response complying with Masing rule.

Increasing the number of nested surfaces enhances the smoothness of the stress–strain response. This follows directly from the fact that each additional surface introduces an extra segment in the piecewise approximation (see Figure 2b), so that in the limit of an infinite number of surfaces the curve tends toward a smooth representation. However, this refinement increases computational cost, since each iteration must handle a larger Jacobian associated with the internal variable updates. In particular, the update equation involves matrix multiplications of size $(6+8N_{\text{act}}) \times (6+8N_{\text{act}})$, where N_{act} denotes the number of active surfaces, as will be explained in more detail in Section 3. For practical applications, a moderate number of surfaces typically achieves an effective balance between accuracy and efficiency. In this work, ten nested surfaces are adopted, which provides this balance and aligns with the number of surfaces commonly used in previous studies [6, 45].

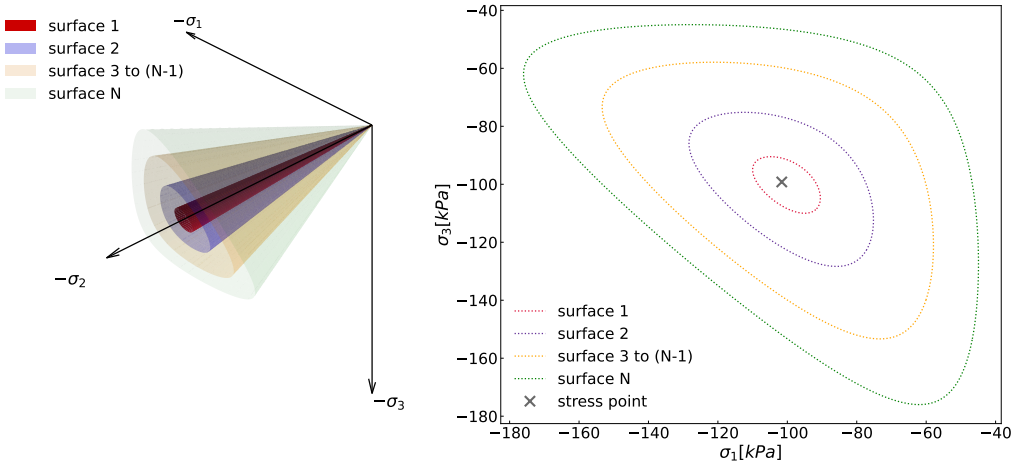

(a)

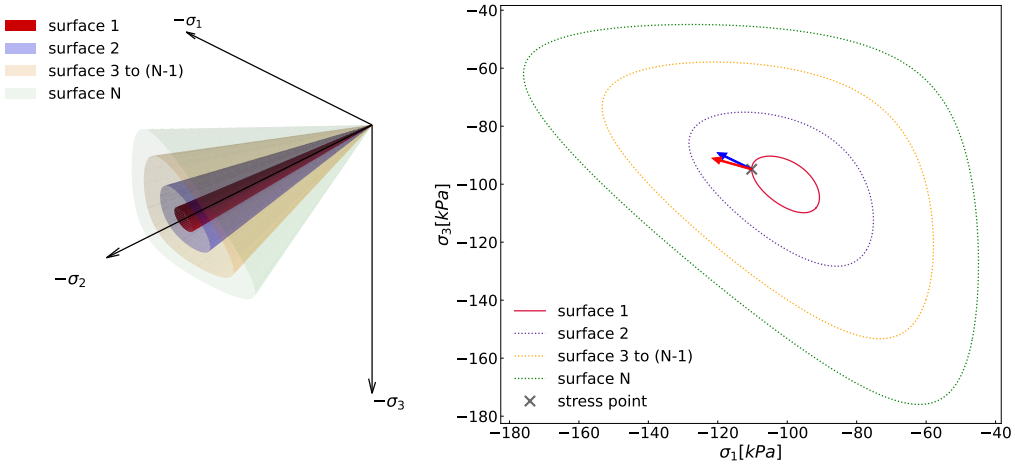

(b)

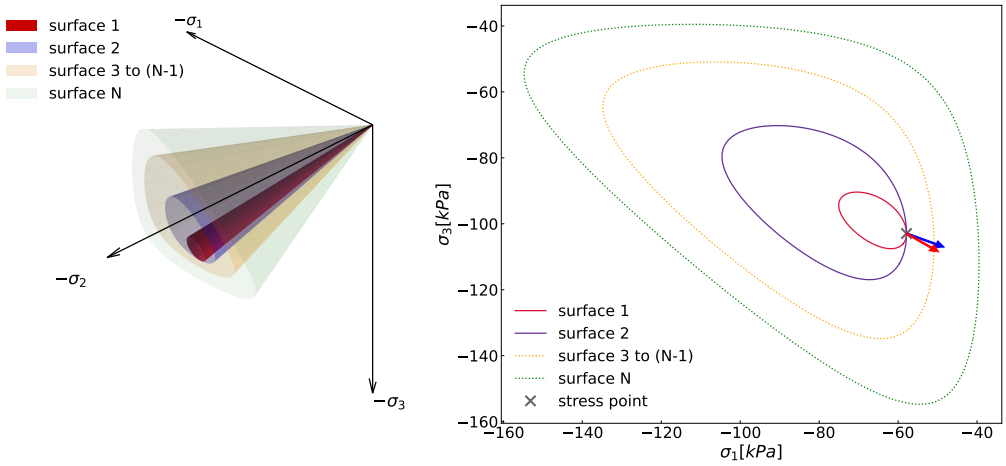

(c)

Figure 3: Evolution of Matsuoka–Nakai nested yield surfaces with kinematic hardening in 3D (left) and 2D (right) stress spaces during triaxial loading: (a) after isotropic consolidation (elastic response), (b) loading, and (c) unloading. Solid lines in the 2D plot represent active yield surfaces at the current loading step. The blue and red arrows indicate the directions of $\boldsymbol{n}$ (Eq. (25)) and $\boldsymbol{m}$ (Eq. (10)).

2.4.1 Hyperplasticity potential functions

The proposed Generalized Cyclic Plasticity (GCP) model embeds non-associative plasticity within hyperplasticity formulation and incorporates combined isotropic-kinematic hardening through a multisurface plasticity model. This allows the evolution of secant stiffness and damping ratio to be captured as cyclic amplitude increases. Kinematic hardening represents the Bauschinger effect, while isotropic hardening accounts for shakedown under repeated cycles [41]. Following the generalized principle of maximum dissipation [50], these mechanisms are unified within a single material model. The formulation is governed by three scalar potentials, which together define the elastic response, plastic flow, and hardening evolution under complex loading conditions, as previously introduced in Section 2.3.

1. Free energy density. The Helmholtz free energy density is expressed in terms of strains and internal variables, allowing for the straightforward calculation of related stresses through derivations [32, 50]. The free energy density with the classical macroscopic elastoplastic approach with micromechanical considerations [32] is given by:

$$\Psi(\boldsymbol{\varepsilon}, \boldsymbol{\varepsilon}^{\mathrm{p}}, \kappa) := \underbrace{\frac{1}{2} \left\| \boldsymbol{\varepsilon} - \boldsymbol{\varepsilon}^{\mathrm{p}} \right\|^2_{\mathbf{C}}}_{\text{elastic}} + \underbrace{\frac{1}{2} \left\| \boldsymbol{\varepsilon}^{\mathrm{p}} \right\|^2_{\mathbf{H}^{\mathrm{kin}}} + \frac{1}{2} (1-b)\, \mathrm{H}^{\mathrm{iso}}\, \kappa^2}_{\text{plastic}} \tag{15}$$

Here, $\mathbf{C}$ is the fourth-order elasticity tensor for isotropic materials, composed of the bulk modulus K and the shear modulus μ:

$$\mathbf{C} = K\, \mathbf{I} \otimes \mathbf{I} + 2\mu \left(\mathbb{I} - \frac{1}{3} \mathbf{I} \otimes \mathbf{I} \right) \tag{16}$$

where $\mathbf{I}$ is the second-order identity tensor, $\mathbb{I}$ is the fourth-order symmetric identity tensor, and $\otimes$ denotes the outer product. This formulation accounts for both volumetric and deviatoric components of kinematic hardening. Kinematic hardening is introduced via the backstress tensor $\boldsymbol{\alpha}$, which describes the center of the translating yield surface. It serves as a material memory mechanism, directly reflecting the loading history [41]. Additionally, it captures shear-induced anisotropy when backstresses vary directionally, such as in triaxial shearing [41]. The generalized stress is derived from the free energy density as:

$$\boldsymbol{s}^{\mathrm{p}} = -\frac{\partial \Psi}{\partial \boldsymbol{\varepsilon}^{p}} = \boldsymbol{\sigma} - \mathbf{H}^{\mathrm{kin}} : \boldsymbol{\varepsilon}^{\mathrm{p}} \tag{17}$$

Given N nested surfaces to describe hardening behavior, the generalized stress for the n^{th} surface ($n \leq N$) is:

$$\boldsymbol{s}^{\mathrm{p}\,(n)} = \boldsymbol{\sigma} - \mathbf{H}^{\mathrm{kin}^{(n)}} : \boldsymbol{\varepsilon}^{\mathrm{p}^{(n)}} = \boldsymbol{\sigma} - \boldsymbol{\alpha}^{(n)} \tag{18}$$

where $\boldsymbol{\sigma}$ is the stress tensor, and $\boldsymbol{\alpha}^{(n)}$ is the backstress for the n^{th} surface, evolving as:

$$\dot{\boldsymbol{\alpha}}^{(n)} = \Delta\lambda^{(n)}\, \mathbf{H}^{\mathrm{kin}^{(n)}} \boldsymbol{m}^{(n)} \tag{19}$$

Here $\Delta\lambda^{(n)}$ is the consistency parameter (Lagrange multiplier) of the n^{th} surface, determined by the Karush-Kuhn-Tucker (KKT) conditions as detailed in Section 3. $\mathbf{H}^{\mathrm{kin}^{(n)}}$ is the fourth-order kinematic hardening tensor for the n^{th} surface defined by its volumetric and deviatoric components:

$$\mathbf{H}^{\mathrm{kin}} = \mathrm{H}^{\mathrm{kin}}_{K} \mathbf{I} \otimes \mathbf{I} + \mathrm{H}^{\mathrm{kin}}_{\mu} \left(\mathbb{I} - \frac{1}{3} \mathbf{I} \otimes \mathbf{I} \right) \tag{20}$$

Isotropic hardening is incorporated via the scalar-valued internal variable κ and its generalized stress conjugate h, both derived in thermodynamic consistency [50]. For the n^{th} surface:

$$\dot{\kappa}^{(n)} = \frac{\partial g^{(n)}}{\partial h^{(n)}} = \frac{\Delta\lambda^{(n)}}{\sqrt{3}}, \qquad h^{(n)} = -(1-b)\, \mathrm{H}^{\mathrm{iso}^{(n)}} \kappa^{(n)}, \qquad \dot{h}^{(n)} = \frac{-\Delta\lambda^{(n)}}{\sqrt{3}} (1-b)\, \mathrm{H}^{\mathrm{iso}^{(n)}} \tag{21}$$

Here, $\mathrm{H}^{\mathrm{iso}^{(n)}}$ is the isotropic hardening modulus of the n^{th} surface, and $b \in [0,1]$ is a parameter controlling the dissipative mechanism. Specifically, $b = 1$ corresponds to a purely dissipative mechanism, while $b = 0$ represents an energetic mechanism that replicates the underlying dissipation. The choice of b is closely tied to thermodynamic consistency. In this study, we adopt $b = 1$ to ensure consistency[50].

2. Yield function. The yield function with combined isotropic-kinematic hardening is defined in terms of the stress, back stress, and isotropic hardening variables. For the n^{th} surface, the yield function is given by:

$$f^{(n)}\left(\boldsymbol{s}^{\mathrm{p}\,(n)}, \kappa^{(n)}\right) \;=\; -C \;+\; A_{\varphi}^{(n)}\, p^{(n)} \;+\; J^{(n)}\,\Gamma\left(\theta^{(n)}\right) + \frac{1}{\sqrt{3}}\,\left(h^{(n)} - \bar{\sigma}^{\mathrm{p}\,(n)}(\kappa^{(n)})\right) \;\leq\; 0 \tag{22}$$

where $p^{(n)}$, $J^{(n)}$, and $\theta^{(n)}$ are computed from $\boldsymbol{s}^{\mathrm{p}\,(n)} = \boldsymbol{\sigma} - \boldsymbol{\alpha}^{\,(n)}$, and

$$\bar{\sigma}^{\mathrm{p}\,(n)}(\kappa^{(n)}) \;=\; \sigma^{p\,(n)} + b\,\mathrm{H}^{\mathrm{iso}^{(n)}}\,\kappa^{(n)} \tag{23}$$

where $\sigma^{p\,(n)}$ is the plastic yield strength of the n^{th} surface for the given material such that:

$$\sigma^{p\,(n)} = \frac{6\,c^{\,(n)}\,\cos\varphi^{\,(n)}}{3 - \sin\varphi^{\,(n)}} \tag{24}$$

Here we define the subdifferential of the yield function with respect to the corresponding generalized stress $\boldsymbol{n}$. For the n^{th} surface:

$$\boldsymbol{n}^{\,(n)} = \frac{\partial f^{\,(n)}}{\partial \boldsymbol{s}^{\mathrm{p}\,(n)}} = \boldsymbol{n}_{\mathrm{dev}}^{(n)} + \boldsymbol{n}_{\mathrm{v}}^{(n)} \tag{25}$$

In the adopted Cauchy stress representation, it is expressed in Voigt notation as a 6×1 vector.

3. Plastic flow potential. The non-associative plastic flow potential shares the same functional form as the yield function as explained in Section 2. For the n^{th} surface, the plastic flow potential is given by:

$$g^{\,(n)}\left(\boldsymbol{s}^{\mathrm{p}\,(n)}, \kappa^{(n)}\right) \;=\; A_{\psi}^{(n)}\, p^{(n)} \;+ J^{(n)}\,\hat{\Gamma}(\theta^{(n)}) + \frac{1}{\sqrt{3}}\,\left(h^{(n)} - \bar{\sigma}^{\mathrm{p}\,(n)}(\kappa^{(n)})\right) \tag{26}$$

The evolution of plastic strain for each surface, $\dot{\boldsymbol{\varepsilon}}^{\mathrm{p}\,(\mathrm{n})}$, is governed by the subdifferential of the plastic potential function with respect to the corresponding generalized stress:

$$\dot{\boldsymbol{\varepsilon}}^{\mathrm{p}\,(\mathrm{n})} \;=\; \Delta\lambda^{\,(n)}\,\frac{\partial g^{\,(n)}}{\partial \boldsymbol{s}^{\mathrm{p}\,(n)}} \;=\; \Delta\lambda^{\,(n)}\,\boldsymbol{m}^{\,(n)} \tag{27}$$

The total plastic strain has the component of all surfaces and is given by:

$$\dot{\boldsymbol{\varepsilon}}^{\mathrm{p}} = \sum_{n=1}^{N} \Delta\lambda^{(n)}\,\boldsymbol{m}^{(n)} \tag{28}$$

2.4.2 Thermodynamical consistency through the generalized principle of maximum dissipation

The GCP model must satisfy the Clausius–Planck inequality to ensure thermodynamic consistency. Following the variational framework of Ulloa et al. [50], the dissipation is defined as:

$$\phi := \boldsymbol{\sigma} : \dot{\boldsymbol{\varepsilon}} - \dot{\Psi}(\boldsymbol{\varepsilon}, \boldsymbol{\varepsilon}^{\mathrm{p}}, \kappa) \geq 0 \tag{29}$$

A state-dependent dissipation potential is introduced by redefining the elastic domain as $\mathbb{L}$ and by employing a continuous support function r. This function bounds the yield surface from above for positive values, leaves it unbounded for negative values, and coincides with g when $f = 0$. For a single surface:

$$r(\boldsymbol{s}^{\mathrm{p}}, \kappa) = g(\boldsymbol{s}^{\mathrm{p}}, \kappa) - f(\boldsymbol{s}^{\mathrm{p}}, \kappa) \tag{30}$$

and the elastic domain is defined as

$$\mathbb{L}(\boldsymbol{s}^{\mathrm{p}}, \kappa) := \left\{ \{\tilde{\boldsymbol{s}}^{\mathrm{p}}, \tilde{\kappa}\} \in \mathbb{R}^{3\times3}_{\mathrm{sym}} \times \mathbb{R} \;\middle|\; g(\tilde{\boldsymbol{s}}^{\mathrm{p}}, \tilde{\kappa}) \leq r(\boldsymbol{s}^{\mathrm{p}}, \kappa) \right\} \tag{31}$$

The generalized principle of maximum dissipation is expressed as a state-dependent optimization problem:

$$\phi\left(\dot{\boldsymbol{\varepsilon}}^{\mathrm{p}}, \dot{\kappa}; \boldsymbol{s}^{\mathrm{p}}\right) = \sup \left\{ \phi \;\middle|\; \{\tilde{\boldsymbol{s}}^{\mathrm{p}}, \tilde{\kappa}\} \in \mathbb{L}(\boldsymbol{s}^{\mathrm{p}}, \kappa) \right\} \tag{32}$$

where $\{\boldsymbol{s}^{\mathrm{p}}, \kappa\}$ maximize the dissipation ϕ over all trial states $\{\tilde{\boldsymbol{s}}^{\mathrm{p}}, \tilde{\kappa}\}$.

Explicit solution of this supremum for the state-dependent domain $\mathbb{L}$ remains unavailable due to the involved nature of the formulation. Nevertheless, the convexity of the yield criterion ensures compliance with the second law of thermodynamics within the generalized standard material framework, thereby guaranteeing thermodynamic consistency without explicitly solving the optimization problem.

2.5 Integration of critical state soil mechanics

The mechanical response of sands is inherently state-dependent, as particle rearrangement during shearing induces volumetric changes that depend on both the current void ratio and the effective confining pressure. These volumetric tendencies control the dilatancy, which in turn influences the stress ratio and, consequently, the mobilized shear strength [24]. In the present formulation, we have shown that the critical state friction angle characterizes the yield function f (Eq. (22)), while a constant dilatation angle is adopted for the flow potential g (Eq. (26)). However, considering a constant dilatancy angle throughout loading cannot account for the continuous evolution of stress and density in sands, which often leads to unrealistic predictions. Consequently, the response is limited to either purely contractive ($\psi < 0$) or purely dilative ($\psi > 0$), or critical state ($\psi = 0$) conditions, and therefore cannot reproduce the phase transformation behavior that is characteristic of granular materials. A realistic description of sand behavior thus requires a constitutive framework in which dilatancy evolves consistently with the evolving soil state.

In this context, several approaches have been proposed to introduce state dependency into soil constitutive models, including peak dilatancy relations [4], state indices based on relative density concepts [55, 21], the state parameter introduced by Been and Jefferies [3], and dilation parameters used in models that employ Lagrange multipliers, such as HySand [45]. Empirical peak dilatancy relations capture the dilative response of dense sands, rather than providing a unified description capable of representing both contractive and dilative behavior. Similarly, in HySand, the dilation ratio governs the shear-induced volumetric changes relative to the critical state, while contractive features are incorporated through a separate consolidation mechanism. State indices provide useful measures of density but do not offer a unified mapping between density, pressure, and dilatancy. In contrast, the state parameter provides a unified description of the contractive and dilative tendencies through a single variable, by relating the current void ratio to its pressure-dependent critical state value. As such, it enables consistent prediction of both contraction and dilation across a wide range of densities and confining pressures [23, 29, 24]. Due to its compact form and physical interpretation, the state parameter approach offers a robust way to embed critical state concepts into constitutive models, and is therefore adopted in this study.

In particular, Been and Jefferies introduced the state parameter as a potential, Ψ, analogous to potential functions used in physics [24]:

$$\Psi = e - e_{\mathrm{c}} \tag{33}$$

The critical state void ratio e_{c}, defined at the current mean effective stress, is expressed using a power-law relationship with mean effective stress [28], such that:

$$e_{\mathrm{c}} = e_{\mathrm{c}0} - \lambda_{\mathrm{c}} \left(p \,/\, p_{\mathrm{atm}} \right)^{\xi} \tag{34}$$

where $e_{\mathrm{c}0}$ is the void ratio at zero pressure, λ_{c} and ξ are critical state constants, and p_{ref} denotes the atmospheric pressure.

2.5.1 Dilation parameter evolution

Jefferies [24] established a physical basis for the relationship between the state parameter Ψ and dilatancy, showing that it can be derived from kinematic considerations of void-ratio evolution rather than being introduced empirically. Within this framework, the limiting dilatancy was shown to be proportional to the state parameter through a material constant χ, which provides a direct link between Ψ and the dilation angle at peak strength:

$$\sin \psi_{\text{peak}} = \frac{-\chi\, \Psi}{2 - \chi\, \Psi/3} \tag{35}$$

The influence of χ on the Ψ–ψ_{peak} relationship is included in Appendix A.

It is important to note, however, that the peak dilation angle obtained from Eq. (35) cannot be used directly in the plastic flow potential. In particular, dense sands associated with a large negative state parameter may exhibit a large peak dilation angle while still undergoing an initial phase of volumetric contraction. Conversely, sands with a smaller peak dilation angle may display more pronounced initial contraction. This indicates that the peak dilation angle alone does not govern the instantaneous volumetric response during loading. To address this, the dilation parameter used in the flow potential is expressed in a regularized form through $\exp(\psi_{\text{peak}})$, ensuring a smooth contribution that remains consistent with observed sand behavior. Similar regularization approaches have been adopted in advanced sand constitutive models such as SANISAND [9]. Expressing the dilation parameter in this regularized form implies that it is no longer interpreted as a geometric angle, but rather as a constitutive parameter.

While the state parameter governs dilatancy and thereby controls the mobilization of peak shear strength through its influence on volumetric response, the incremental volumetric behavior during loading is governed by the position of the stress path relative to the phase transformation (PT) line. In the present formulation, the PT condition is introduced in terms of the stress ratio difference $\eta - \bar{\eta}$, where $\eta = q/p$ and $\bar{\eta}$ denotes the phase transformation stress ratio for the given loading direction. Since experimental evidence indicates that the PT condition in sands corresponds to a distinct locus in the p–q plane, stress ratios below $\bar{\eta}$ are associated with contractive behavior, whereas stress ratios above it correspond to dilative behavior. Experimental triaxial observations further show that the PT stress ratio varies systematically with sand density [53]. To represent this dependency in a simple and continuous manner, the PT stress ratio is here expressed as a state-dependent scaling of the critical-state stress ratio M such that:

$$\bar{\eta} = M\, \exp\left(\Psi\right) \tag{36}$$

This expression is not intended as a derivation of the PT condition, but rather as a phenomenological representation introduced to capture the observed shift of the PT locus with density while maintaining a smooth formulation suitable for numerical integration. To ensure a gradual transition between contractive and dilative regimes, the resulting PT condition is embedded within a smooth transition function:

$$w_{\text{PTL}} = \tanh\left(\frac{\eta - \bar{\eta}}{\eta_0}\right) \tag{37}$$

such that w_{PTL} varies continuously from -1 (contractive) to $+1$ (dilative) as the stress ratio traverses the PT line. The parameter $\eta_0 = 0.2$ controls the smoothness of this transition and is introduced as a numerical regularization parameter, rather than a soil-specific material constant. This treatment is consistent with critical-state-based sand models, in which the constitutive response across phase transformation is formulated to remain continuous [23, 9].

To improve calibration of the strain evolution, an additional scaling parameter n_χ is introduced in the dilation parameter. The state-dependent relationship between peak dilatancy and the state parameter is retained through Eq. (35); however, the material constant χ is fixed to unity to remove its scaling role, which is instead absorbed into n_χ. This approach provides better control over the magnitude of dilative and contractive strain evolution, while preserving the physical interpretation of the state-controlled peak

dilatancy. The dilation parameter employed in the plastic flow potential g (Eq. (26)) is finally constructed as:

$$\bar{\psi} = n_\chi \, \exp(\psi_{\text{peak}}) \, w_{\text{PTL}} \tag{38}$$

In combination with appropriate calibration of the hardening parameters, this formulation provides a smooth, state-dependent description of volumetric response while reproducing realistic sand behavior under monotonic and cyclic loading.

2.5.2 Stiffness degradation and state-dependent kinematic hardening

In classical multisurface plasticity models for sands, the constitutive response under undrained cyclic loading often exhibits unrealistically stiff stress–strain loops in the cyclic mobility regime [45]. Once the maximum shear stress is reached and the loading direction reverses, the response becomes prematurely elastic, followed by repeated reactivation of the nested yield surfaces with their full kinematic hardening capacity. As a result, the stress path remains confined within a narrow region of stress space and does not fully develop toward the apex, leading to locked hysteresis loops and insufficient shear strain accumulation during cyclic mobility. To reproduce more realistic cyclic degradation behavior and allow for progressive strain accumulation under repeated loading, a simple stiffness degradation mechanism is introduced in the model.

A scalar degradation factor $d_f \in [0, 1]$ is coupled to the kinematic hardening modulus to represent the progressive loss of stiffness under cyclic loading. The formulation follows the general philosophy of strain-based degradation mechanisms adopted in post-liquefaction sand models, including the strain liquefaction factor in SANISAND–MSf [56] and cumulative plastic shear strain measures used in PM4Sand [5]. Degradation is activated only under low effective stress conditions and evolves as a function of accumulated plastic shear strain according to:

$$\dot{d}_f = n_h \, J_{2\dot{\boldsymbol{\varepsilon}}^{\boldsymbol{p}}} \left(1 - d_f\right)^2 \qquad \text{for } p' < p_{\text{degradation}} \tag{39}$$

where n_h controls the rate of degradation. The quadratic factor $\left(1 - d_f\right)^2$ ensures rapid initiation of degradation at small values of d_f, followed by gradual saturation as $d_f \to 1$, representing a smooth transition toward a strongly degraded cyclic mobility regime. The degradation threshold is estimated geometrically as $p_{\text{degradation}} = M_e \, q_{\text{cyc}}$. As plastic shearing accumulates under low mean effective stress, d_f progressively reduces the effective kinematic hardening capacity, promoting cyclic stiffness degradation and enhanced cyclic mobility.

In addition, kinematic hardening is formulated as state dependent through an explicit function of the state parameter, consistent with recent developments in state-dependent sand models [9, 45]. The dependence of the kinematic hardening modulus on the soil state is introduced through:

$$w_e = \exp(-\Psi)^{\,n_e} \tag{40}$$

where n_e controls the sensitivity of the hardening response to the soil state. The combined effect of density state and cyclic degradation is introduced by scaling the kinematic hardening modulus as:

$$\bar{H}_{\text{kin}} = H_{\text{kin}} \, w_e \left(1 - d_f\right) \tag{41}$$

where H_{kin} denotes the reference kinematic hardening modulus in the absence of state and degradation effects.

3 Numerical implementation

This section outlines the numerical implementation of the constitutive model, building on the implicit integration framework for non-standard plasticity [14, 10]. A fully implicit return-mapping scheme is presented together with the derivation of the combined hardening modulus for multisurface plasticity and the algorithmic procedures used in the triaxial and direct simple shear simulations.

3.1 Implicit return mapping algorithm

Stresses are expressed in Voigt notation as $\boldsymbol{\sigma} = \{\sigma_{xx}, \sigma_{yy}, \sigma_{zz}, \sigma_{xy}, \sigma_{yz}, \sigma_{zx}\}^{\mathrm{T}}$. A fully implicit backward Euler integration scheme is employed within the Closest Point Projection Method (CPPM) to solve the set of linearized equations at each Gauss point. Although the model is rate-independent, the equations are discretized over a finite deformation increment $\Delta\varepsilon$, corresponding to a time step Δt, to maintain the temporal sequence [10]. This approach assumes a linear variation of $\Delta\sigma$ between t_n and t_{n+1}, consistent with the basic Euler scheme.

The rate equations are expressed as a residual vector $\mathbf{r}$ at the integration-point level, which incorporates stresses, hardening variables, and consistency conditions:

$$\mathbf{r}_{\boldsymbol{\sigma}} = \boldsymbol{\sigma} - \boldsymbol{\sigma}^{trial} + \mathbf{C}\dot{\boldsymbol{\varepsilon}}^{p} = \boldsymbol{\sigma} - \boldsymbol{\sigma}^{trial} + \mathbf{C}\sum_{n=1}^{N} \Delta\lambda^{(n)}\, \boldsymbol{m}^{(n)} \tag{42}$$

$$\mathbf{r}_{\boldsymbol{\alpha}}^{(n)} = \boldsymbol{\alpha}^{(n)} - \boldsymbol{\alpha}^{trial\,(n)} - \dot{\boldsymbol{\alpha}}^{(n)} = \boldsymbol{\alpha}^{(n)} - \boldsymbol{\alpha}^{trial\,(n)} - \Delta\lambda^{(n)}\, \mathbf{H}^{\mathrm{kin}^{(n)}} \boldsymbol{m}^{(n)} \tag{43}$$

$$\mathrm{r}_{h}^{(n)} = h^{(n)} - h^{trial\,(n)} - \dot{h}^{(n)} = h^{(n)} - h^{trial\,(n)} - \frac{\Delta\lambda^{(n)}}{\sqrt{3}}\,(1-b)\,\mathrm{H}^{\mathrm{iso}^{(n)}} \tag{44}$$

$$\mathrm{r}_{f}^{(n)} = f\left(\boldsymbol{\sigma}, \boldsymbol{\alpha}^{(n)}, h^{(n)}\right) = -C^{(n)} + A_{\varphi}^{(n)}\, p^{(n)} + J^{(n)}\,\Gamma\left(\theta^{(n)}\right) + \frac{1}{\sqrt{3}}\left(h^{(n)} - \bar{\sigma}^{(n)}\right) \tag{45}$$

Within the multisurface plasticity framework, the residual vector is extended to include contributions from all active yield surfaces N_{act}. For $N_{\mathrm{act}} \leq N$, the Newton-Raphson update equation becomes:

$$\underbrace{\begin{Bmatrix} \Delta\boldsymbol{\sigma} \\ \Delta\boldsymbol{\alpha} \\ \Delta h \\ \Delta\lambda \end{Bmatrix}}_{\Delta\boldsymbol{x}} = -\,\omega\, \underbrace{\begin{bmatrix} \frac{\partial \mathbf{r}_{\boldsymbol{\sigma}}}{\partial \boldsymbol{\sigma}}\,(6\times 6) & \frac{\partial \mathbf{r}_{\boldsymbol{\sigma}}}{\partial \boldsymbol{\alpha}}\,(6\times 6N_{\mathrm{act}}) & \frac{\partial \mathbf{r}_{\boldsymbol{\sigma}}}{\partial h}\,(6\times N_{\mathrm{act}}) & \frac{\partial \mathbf{r}_{\boldsymbol{\sigma}}}{\partial \Delta\lambda}\,(6\times N_{\mathrm{act}}) \\ \frac{\partial \mathbf{r}_{\boldsymbol{\alpha}}}{\partial \boldsymbol{\sigma}}\,(6N_{\mathrm{act}}\times 6) & \frac{\partial \mathbf{r}_{\boldsymbol{\alpha}}}{\partial \boldsymbol{\alpha}}\,(6N_{\mathrm{act}}\times 6N_{\mathrm{act}}) & \frac{\partial \mathbf{r}_{\boldsymbol{\alpha}}}{\partial h}\,(6N_{\mathrm{act}}\times N_{\mathrm{act}}) & \frac{\partial \mathbf{r}_{\boldsymbol{\alpha}}}{\partial \Delta\lambda}\,(6N_{\mathrm{act}}\times N_{\mathrm{act}}) \\ \frac{\partial \mathrm{r}_{h}}{\partial \boldsymbol{\sigma}}\,(N_{\mathrm{act}}\times 6) & \frac{\partial \mathrm{r}_{h}}{\partial \boldsymbol{\alpha}}\,(N_{\mathrm{act}}\times 6N_{\mathrm{act}}) & \frac{\partial \mathrm{r}_{h}}{\partial h}\,(N_{\mathrm{act}}\times N_{\mathrm{act}}) & \frac{\partial \mathrm{r}_{h}}{\partial \Delta\lambda}\,(N_{\mathrm{act}}\times N_{\mathrm{act}}) \\ \frac{\partial \mathrm{r}_{f}}{\partial \boldsymbol{\sigma}}\,(N_{\mathrm{act}}\times 6) & \frac{\partial \mathrm{r}_{f}}{\partial \boldsymbol{\alpha}}\,(N_{\mathrm{act}}\times 6N_{\mathrm{act}}) & \frac{\partial \mathrm{r}_{f}}{\partial h}\,(N_{\mathrm{act}}\times N_{\mathrm{act}}) & \frac{\partial \mathrm{r}_{f}}{\partial \Delta\lambda}\,(N_{\mathrm{act}}\times N_{\mathrm{act}}) \end{bmatrix}^{-1}}_{\boldsymbol{J}_{(6+8N_{\mathrm{act}}\times 6+8N_{\mathrm{act}})}} \underbrace{\begin{Bmatrix} \mathbf{r}_{\boldsymbol{\sigma}} \\ \mathbf{r}_{\boldsymbol{\alpha}} \\ \mathrm{r}_{h} \\ \mathrm{r}_{f} \end{Bmatrix}}_{\mathbf{r}} \tag{46}$$

In the equation above, ω denotes the line search parameter and $\boldsymbol{J}$ the Jacobian matrix. Due to the limited convergence radius of Newton-Raphson methods, a fixed ω (i.e., $\omega = 1$) may cause convergence to a local minimum. The Armijo backtracking line search [2] is employed to improve global convergence in the cases of bad convergence so that ω is adaptively selected to ensure sufficient decrease in the residual norm and energy, helping the stress point escape local minima.

3.2 Derivation of combined hardening modulus under multisurface plasticity

This subsection addresses the enforcement of consistency conditions across multiple yield surfaces within the implicit integration framework. The formulation ensures that all active surfaces satisfy the KKT conditions simultaneously. There are various methodologies for implementing multisurface plasticity. The Mroz translation approach [37], as used in the models developed by Prevost [43, 42], requires identifying the active outermost surface. This may result in discontinuities caused by abrupt changes in the direction of plastic strain direction [6]. In contrast, Prager's approach [36] utilizes the innermost surface to govern the evolution equations, thereby reducing model complexity and avoiding such discontinuities [6]. Both approaches involve determining the direction of surface translation and relocating surfaces based on the active one. In the present study, however, all surfaces are updated based on the KKT conditions, ensuring consistency at each strain increment across all surfaces.

Once the active surfaces are identified, the primary variables are solved simultaneously at the integration point using a Newton-Raphson scheme [14]. The nonlinear system in Eq. (46) is iterated until the

residuals are sufficiently small, thereby satisfying the local KKT conditions. The consistency condition for the n^{th} surface gives:

$$\dot{f}^{\,(n)} = \frac{\partial f^{\,(n)}}{\partial \boldsymbol{\sigma}} \, \dot{\boldsymbol{\sigma}} + \frac{\partial f^{\,(n)}}{\partial \boldsymbol{\alpha}^{\,(n)}} \, \dot{\boldsymbol{\alpha}}^{\,(n)} + \frac{\partial f^{\,(n)}}{\partial h^{\,(n)}} \, \dot{h}^{\,(n)} + \frac{\partial f^{\,(n)}}{\partial \kappa^{\,(n)}} \, \dot{\kappa}^{\,(n)} = 0 \tag{47}$$

By combining Eq. (47) with Eq. (28), the stress increment is derived as:

$$\dot{\boldsymbol{\sigma}} = \mathbf{C} \, (\dot{\boldsymbol{\varepsilon}} - \dot{\boldsymbol{\varepsilon}}^{\mathrm{p}}) = \mathbf{C} \left(\dot{\boldsymbol{\varepsilon}} - \sum_{i=1}^{N} \Delta\lambda^{(i)} \, \boldsymbol{m}^{(i)} \right) \tag{48}$$

Eq. (47) can be rewritten by inserting Eq. (48) and Eq. (25) and hardening laws:

$$\dot{f}^{\,(n)} = \boldsymbol{n} \, \mathbf{C} \left(\dot{\boldsymbol{\varepsilon}} - \sum_{i=1}^{N} \Delta\lambda^{(i)} \, \boldsymbol{m}^{(i)} \right) - \boldsymbol{n} \, \Delta\lambda^{(n)} \, \mathbf{H}^{\mathrm{kin}^{(n)}} \boldsymbol{m}^{(n)} - \Delta\lambda^{(n)} \, \frac{\mathbf{H}^{\mathrm{iso}^{(n)}}}{3} = 0 \tag{49}$$

For all surfaces, the first term in Eq. (49) is shared. This means that for different surfaces the sum of hardening terms (second and third terms in Eq. (49)) should be equal, such that:

$$\boldsymbol{n} \, \Delta\lambda^{(n+1)} \, \mathbf{H}^{\mathrm{kin}^{(n+1)}} \boldsymbol{m} + \Delta\lambda^{(n+1)} \, \frac{\mathbf{H}^{\mathrm{iso}^{(n+1)}}}{3} = \boldsymbol{n} \, \Delta\lambda^{(n)} \, \mathbf{H}^{\mathrm{kin}^{(n)}} \boldsymbol{m} + \Delta\lambda^{(n)} \, \frac{\mathrm{H}^{\mathrm{iso}^{(n)}}}{3} \tag{50}$$

Therefore, the consistency parameter for any surface can be defined by the consistency parameter of any other surface as:

$$\Delta\lambda^{(n+1)} = \Delta\lambda^{(n)} \, \frac{\boldsymbol{n} \, \mathbf{H}^{\mathrm{kin}^{(n)}} \boldsymbol{m} + \mathrm{H}^{\mathrm{iso}^{(n)}}/3}{\boldsymbol{n} \, \mathbf{H}^{\mathrm{kin}^{(n+1)}} \boldsymbol{m} + \mathrm{H}^{\mathrm{iso}^{(n+1)}}/3} = \Delta\lambda^{(n)} \, \frac{\overline{h}^{(n)}}{\overline{h}^{(n+1)}} \tag{51}$$

where we define $\overline{h}^{(n)}$ as the hardening modulus of the n^{th} surface. Inserting this dependency into Eq. (48) would give:

$$\dot{\boldsymbol{\sigma}} = \mathbf{C} \left(\dot{\boldsymbol{\varepsilon}} - \boldsymbol{m} \, \Delta\lambda^{(1)} \, \overline{h}^{(1)} \sum_{i=1}^{N} \frac{1}{\overline{h}^{(i)}} \right) \tag{52}$$

If $\dot{\boldsymbol{\sigma}}$ in Eq. (52) is substituted in Eq. (49), we get:

$$\dot{f}^{\,(n)} = \boldsymbol{n} \, \mathbf{C} \left(\dot{\boldsymbol{\varepsilon}} - \boldsymbol{m} \, \Delta\lambda^{(1)} \, \overline{h}^{(1)} \sum_{i=1}^{N} \frac{1}{\overline{h}^{(i)}} \right) - \boldsymbol{n} \, \Delta\lambda^{(n)} \, \mathbf{H}^{\mathrm{kin}^{(n)}} \boldsymbol{m} - \Delta\lambda^{(n)} \, \frac{\mathbf{H}^{\mathrm{iso}^{(n)}}}{3} = 0 \tag{53}$$

From here, we can get the consistency parameter for the first surface $\Delta\lambda^{(1)}$:

$$\Delta\lambda^{(1)} = \frac{\boldsymbol{n} \, \mathbf{C} \dot{\boldsymbol{\varepsilon}}}{\boldsymbol{n} \, \mathbf{C} \boldsymbol{m} \, \overline{h}^{(1)} \, \sum_{i=1}^{N} \frac{1}{\overline{h}^{(i)}} + \overline{h}^{(1)}} \tag{54}$$

Plugging $\Delta\lambda^{(1)}$ into Eq. (52) gives:

$$\dot{\boldsymbol{\sigma}} = \mathbf{C} \left(\dot{\boldsymbol{\varepsilon}} - \boldsymbol{m} \, \frac{\boldsymbol{n} \, \mathbf{C} \dot{\boldsymbol{\varepsilon}}}{\boldsymbol{n} \, \mathbf{C} \boldsymbol{m} + \dfrac{1}{\sum_{n=i}^{N} \frac{1}{\overline{h}^{(i)}}}} \right) = \dot{\boldsymbol{\varepsilon}} \left(\mathbf{C} - \frac{(\mathbf{C} \cdot \boldsymbol{m}) \otimes (\boldsymbol{n} \cdot \mathbf{C})}{\boldsymbol{n} \, \mathbf{C} \boldsymbol{m} + \dfrac{1}{\sum_{n=i}^{N} \frac{1}{\overline{h}^{(i)}}}} \right) \tag{55}$$

Eq. (55) clearly shows that the consistent tangent operator, $\mathbf{C}^{\mathbf{ep}}$ reflects the combined effect of all active yield surfaces and is given by:

$$\mathbf{C}^{\mathbf{ep}} = \mathbf{C} - \frac{(\mathbf{C} \cdot \boldsymbol{m}) \otimes (\boldsymbol{n} \cdot \mathbf{C})}{\boldsymbol{n} \, \mathbf{C} \boldsymbol{m} + \tilde{h}} \tag{56}$$

where $\tilde{h}$ is the hardening modulus of the system consisting the contribution of all active surfaces, resembling springs connected in series. For N_{act} active surfaces:

$$\frac{1}{\tilde{h}} = \sum_{i=1}^{N_{\text{act}}} \frac{1}{h^{(i)}} = \frac{1}{h^{(1)}} + \frac{1}{h^{(2)}} + ... + \frac{1}{h^{(N_{\text{act}})}} \tag{57}$$

By expressing the combined hardening response as an equivalent modulus derived from the interaction of individual surfaces, the approach reveals an intuitive analogy to springs connected in series (see Figure 2a). This interpretation provides insight into how multisurface hardening influences the overall stiffness and stress update in cyclic plasticity models (see Figure 2b).

3.3 Simulations of triaxial and direct simple shear tests

A series of element-level simulations, including triaxial and direct simple shear (DSS) tests, is carried out to evaluate the predictive capabilities of the proposed GCP model. These simulations are compared against characteristic experimental trends reported in the literature and results from established constitutive models, thereby offering a systematic evaluation of the model's ability to reproduce characteristic features of sand behavior. The analyses consider both isotropic and anisotropic consolidation conditions, followed by controlled loading, as illustrated in Figure 4. Isotropic consolidation is imposed by incrementally applying the hydrostatic pressure p_0. In the case of anisotropic consolidation, an additional deviatoric stress q_0 is introduced while maintaining a constant mean effective pressure p_0. Undrained conditions are imposed by enforcing incompressibility through the condition $\Delta\varepsilon_v = \Delta\varepsilon_{xx} + \Delta\varepsilon_{yy} + \Delta\varepsilon_{zz} = 0$. For triaxial tests, this leads to the strain-increment relation $\Delta\varepsilon_{yy} = \Delta\varepsilon_{zz} = -0.5\,\Delta\varepsilon_{xx}$, whereas for direct simple shear (DSS) tests the constraint is enforced by prescribing zero normal strain increments, such that $\Delta\varepsilon_{xx} = \Delta\varepsilon_{yy} = \Delta\varepsilon_{zz} = 0$. Under these conditions, the void ratio e remains constant, while the critical void ratio e_{c} evolves during shearing.

Although the GCP model is rate independent, sufficiently small strain increments are used to improve the robustness of the Newton iterations, particularly under highly nonlinear response. If convergence is not achieved for a given load step, a substepping procedure is employed in which the strain increment is progressively reduced until a prescribed minimum admissible axial strain increment $\Delta\varepsilon_{xx}$ is reached. The implicit return-mapping algorithm employed for these simulations is presented in Appendix C.

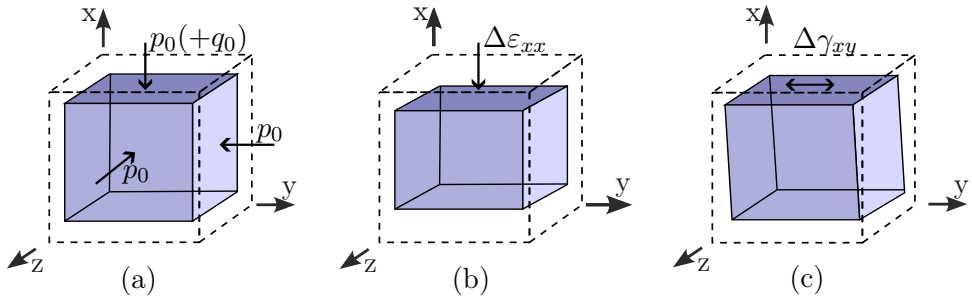

Figure 4: Schematic representation of the loading applied in the element-level numerical simulations. Dashed lines denote the initial configuration and the solid blue cube the deformed configuration. Applied stress and strain increments on the cube faces illustrate the loading paths for (a) isotropic and anisotropic consolidation, (b) triaxial test, and (c) direct simple shear test.

4 Verification of the proposed model

The proposed GCP model is verified against the established Prevost model for cohesionless soils [42], using Nevada sand parameters calibrated and triaxial test simulations reported by Cerfontaine [6]. To reproduce the Prevost formulation, the GCP model is configured with pressure-dependent kinematic hardening, and

a phase transformation-based dilatancy rule, while isotropic hardening is deactivated. This configuration provides a consistent benchmark for assessing the ability of the GCP model to recover classical cyclic soil behavior.

4.1 Prevost model implementation within the GCP model

The Prevost model employs purely deviatoric and pressure-dependent kinematic hardening, which introduces directional memory and ensures that cyclic stress paths pass through the origin in mobility plots. The yield surface for the n^{th} surface is given by:

$$f\left(\boldsymbol{\sigma}, \boldsymbol{\alpha}^{(n)}\right) \;=\; f\left(\boldsymbol{s}^{\mathrm{p}\,(n)}\right) \;=\; \frac{3}{2}\left(\boldsymbol{\sigma}_{\text{dev}} - p\,\boldsymbol{\alpha}^{(n)}\right) : \left(\boldsymbol{\sigma}_{\text{dev}} - p\,\boldsymbol{\alpha}^{(n)}\right) - \left(p\,M^{(n)}\right)^2 \tag{58}$$

Since the yield function in Eq. (58) is quadratic in the stress, the associated consistency equation admits two real solutions in the vicinity of the apex. This multiplicity yields two admissible return-mapping directions, which is a well-known source of numerical difficulty because the projection of the trial stress onto the yield surface is no longer unique. As discussed in Panteghini and Lagioia (2014), yield functions that allow multiple roots for a given stress state may exhibit non-unique stress updates and loss of convergence as the mean stress approaches zero. Cerfontaine [6] showed that these issues can be mitigated by introducing a small artificial cohesion, which shifts the apex of the yield surface so that the stress update can be performed in this regularized space before being mapped back to the original configuration. Even with such regularization, however, implicit integration may still lose convergence before p reaches zero, as documented in their simulations [6].

Within the generalized yield-surface framework, the classical Prevost yield surface of Eq. (58) is reproduced by selecting the Drucker–Prager shape function parameters (Table 1), with the friction parameter for each surface given by:

$$M^{(n)} = \sqrt{3}\,A_{\varphi}^{(n)} \tag{59}$$

Kinematic hardening law

The pressure-dependent kinematic hardening law for the n^{th} surface is expressed as:

$$\dot{\boldsymbol{\alpha}}^{(n)}\,p = \Delta\lambda^{(n)}\,\mathbf{H}_{\mu}^{\mathrm{kin}^{(n)}}\,\boldsymbol{m}_{\text{dev}}^{(n)} \tag{60}$$

leading to the residual form:

$$\mathbf{r}_{\boldsymbol{\alpha}}^{(n)} = \boldsymbol{\alpha}^{(n)} - \boldsymbol{\alpha}^{trial\,(n)} - \dot{\boldsymbol{\alpha}}^{(n)} = \boldsymbol{\alpha}^{(n)} - \boldsymbol{\alpha}^{trial\,(n)} - \frac{\Delta\lambda^{(n)}\,\mathbf{H}_{\mu}^{\mathrm{kin}^{(n)}}\boldsymbol{m}_{\text{dev}}^{(n)}}{p} \tag{61}$$

The elements of the Jacobian are provided in Appendix B in closed form. Surface moduli $\mathrm{H}^{(n)}$ are obtained from the cumulative Prevost moduli $\mathrm{H}'^{(n)}$ through:

$$\frac{1}{\mathrm{H}^{(n)}} = \frac{1}{\mathrm{H}'^{\,(n)}} - \frac{1}{\mathrm{H}'^{\,(n-1)}}, \quad \text{where} \quad n = 2, \ldots, N \qquad \mathrm{H}^{(1)} = \mathrm{H}'^{(1)} \tag{62}$$

A purely deviatoric backstress tensor is employed:

$$\boldsymbol{\alpha} = \frac{\alpha}{3}\begin{bmatrix} 2 & 0 & 0 \\ 0 & -1 & 0 \\ 0 & 0 & -1 \end{bmatrix} \tag{63}$$

Dilatancy formulation

The Prevost model defines the onset of dilatancy through the phase transformation (PT) ratio $\bar{\eta}$. Although this introduces volumetric plasticity, the formulation does not include a state parameter and therefore cannot capture convergence toward the critical state. The plastic flow direction is decomposed into an associated deviatoric component $\boldsymbol{m}_{\text{dev}} = \dfrac{\boldsymbol{n}_{\text{dev}}}{\|\boldsymbol{n}_{\text{dev}}\|}$ and a non-associated volumetric component $\boldsymbol{m}_{\text{v}} = m_{\text{v}}\,\mathbf{I}$. Governed by Prevost's dilatancy rule, m_{v} is expressed in terms of the current stress ratio η and the PT ratio $\bar{\eta}$, allowing positive and negative values to produce dilation and contraction, respectively, such that:

$$m_{\text{v}} = \frac{\bar{\eta}^2 - \eta^2}{\bar{\eta}^2 + \eta^2} \tag{64}$$

4.2 Verification against reported triaxial test simulations

The Prevost model parameters calibrated for Nevada sand are adopted from Cerfontaine [6]. Elastic reference parameters and the PT ratio are given in Table 2, and the strength and hardening parameters of the Prevost yield surfaces are given in Table 3.

Table 2: Prevost model elastic reference parameters and PT ratio for Nevada sand calibrated by Cerfontaine [6]

μ_{ref} [MPa]	K_{ref} [MPa]	p_{ref} [kPa]	β [-]	$\bar{\eta}$ [-]
40	66.67	-100	0	0.8

Table 3: Prevost model yield surface and hardening parameters for Nevada sand calibrated for nine surfaces by Cerfontaine [6]

	unit	1	2	3	4	5	6	7	8	9
M	-	0.08	0.15	0.3	0.425	0.64	0.775	0.92	1.045	1.14
$\mathrm{H}_{\mu}^{\text{kin}}$	MPa	150	300	43	15	2.5	2.0	0.67	0.24	0.011
α	-	0	0.05	0.1	0.175	0.26	0.225	0.22	0.155	0.14

Undrained cyclic triaxial loading is applied in the form $q = q_0 \pm q_{\text{cycl}}$, with a fixed relative density of 40%, a consolidation pressure of $p_0 = -250$ kPa, and two initial deviatoric stresses, $q_0 = -30$ kPa and $q_0 = -45$ kPa with the same cyclic amplitude of 40 kPa. Comparisons between the proposed GCP model and Cerfontaine's implicit implementation of the Prevost model are shown in Figure 5. The two simulations exhibit distinct undrained cyclic behaviors because the combination of the initial deviatoric stress and the applied cyclic stress amplitude places the loading paths in different regions of the stress space. For the case of $q = -45 \pm 40$ kPa (Figures 5a and 5b), the response develops stable, closed cyclic loops with a dilative tendency and limited pore-pressure accumulation. In contrast, for the case of $q = -30 \pm 40$ kPa (Figures 5c and 5d), the loading path is driven toward the extension side, where pore pressure rises rapidly and the mean effective stress approaches zero, resulting in a cyclic-mobility response. In both cases, the GCP model reproduces the key response features of the Prevost model. Minor offsets in Figures 5b and 5d arise from the error control applied in the reference solution. The reference simulation [6] loses convergence before the stress path reaches the apex, and the final converged step is marked in Figure 5c with an arrow. In contrast, the GCP formulation remains stable in this region due to its numerically robust yield-surface structure.

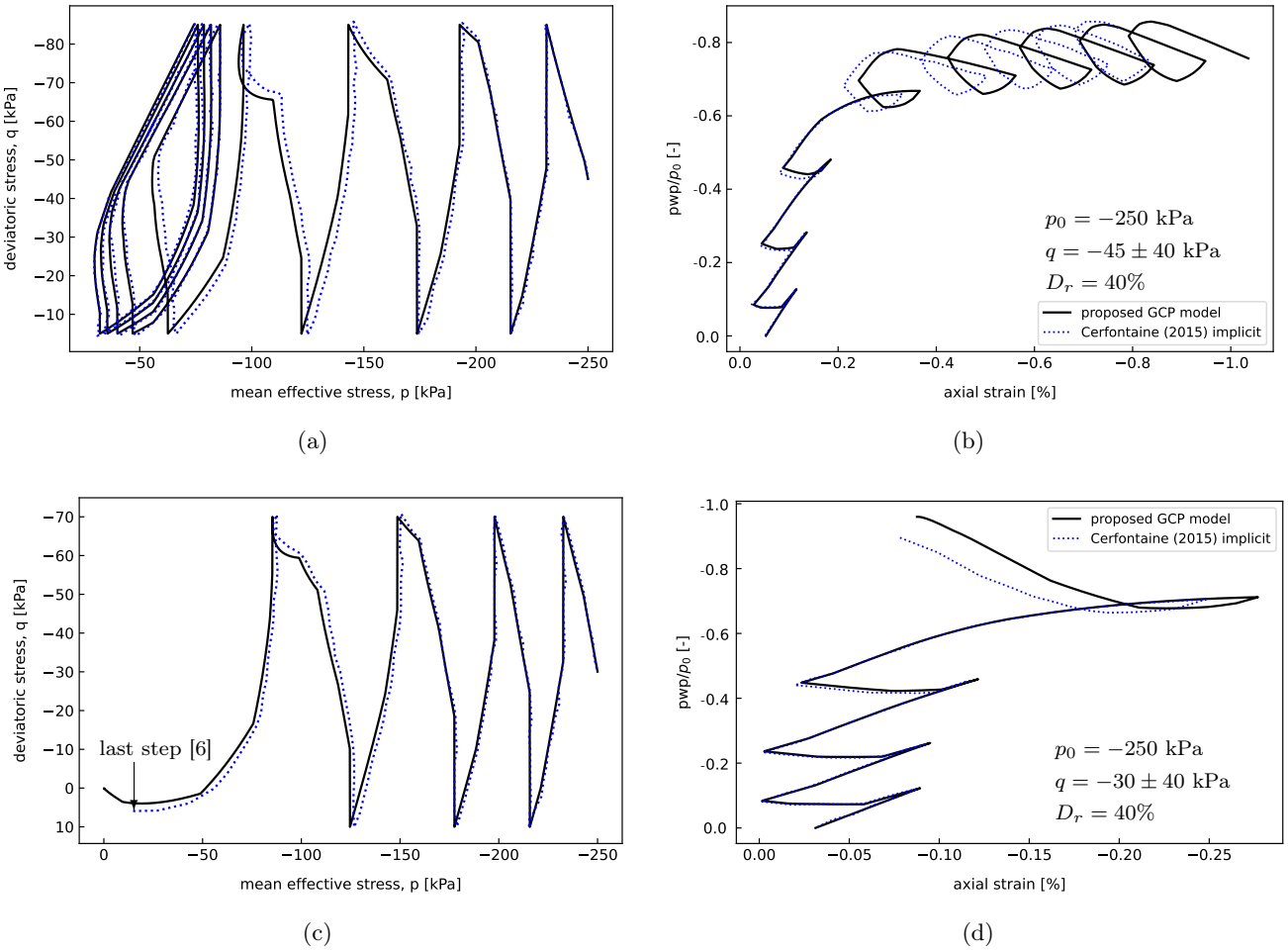

Figure 5: Undrained cyclic triaxial test simulations with relative density $D_r = 40\%$ and consolidation pressure $p_0 = -250$ kPa. The top row corresponds to initial deviatoric stress $q_0 = -45$ kPa, and the bottom row corresponds to $q_0 = -30$ kPa. (a)–(c) Deviatoric stress q plotted against mean effective stress p and (b)–(d) normalized excess pore water pressure plotted against axial strain. The final converged step of the reference simulation [6] is indicated in (c) with an arrow.

5 Capabilities and versatility of the proposed model

This section demonstrates the capabilities and versatility of the proposed GCP model in capturing the complex response of sands under both monotonic and cyclic loading. The model employs twelve primary parameters, all of which can calibrated from standard laboratory tests. With this compact parameter set, the GCP model captures a wide range of characteristic soil behaviors, including excess pore pressure generation, cyclic mobility, stiffness and damping evolution with increasing number of cycles, Lode angle dependency, shakedown through combined hardening, and dilation and contraction through non-associative flow within the CSSM framework.

5.1 GCP model parameters

The GCP model is formulated using a set of soil parameters that correspond directly to measurable features of sand behavior. Each parameter reflects a specific aspect of the material response such as elastic stiffness, critical state characteristics, or the evolution of plastic hardening, which can be calibrated from standard laboratory tests. Table 4 summarizes the full list of parameters together with their physical meaning, units, and recommended calibration tests.

Table 4: GCP model parameters, units, description, and recommended calibration tests

Component	Parameter	Unit	Description	Calibration Test
Elasticity	μ_{ref}	kPa	Shear modulus at reference pressure	Drained triaxial or bender element test
	K_{ref}	kPa	Bulk modulus at reference pressure	Drained triaxial or resonant column test
Critical state	λ_{c}	–	Slope of critical state line in e–$\ln p$ space	Isotropic compression or consolidation test
	ξ	–	Critical state line constant	Isotropic compression or consolidation test
	e_{c0}	–	Void ratio at zero pressure	Isotropic compression or consolidation test
	n_χ	–	Dilation parameter material constant	Drained or undrained triaxial at different densities
	M_c or φ_{c}	–, °	CS stress ratio or friction angle	Drained or undrained triaxial compression
	M_e	–	CS stress ratio for extension	Drained or undrained triaxial extension
Hardening	h_μ^{kin}	kPa	Shear kinematic hardening modulus	Monotonic triaxial test
	b	–	Exponent controlling hardening for surfaces	Monotonic triaxial test
	n_e	–	Exponent controlling hardening across soil states	Monotonic triaxial test at different soil states
	n_h	–	Exponent controlling stiffness degradation	Undrained cyclic triaxial tests
Optional	h_K^{kin}	kPa	Bulk kinematic hardening modulus (default 0)	Cyclic triaxial test
	h^{iso}	kPa	Isotropic hardening modulus (default 0)	Cyclic triaxial tests with accumulated plastic strain
	N	–	Number of yield surfaces (default 10)	Numerical choice
	c	kPa	Effective cohesion (default 0)	Direct shear test
	β	–	Elasticity confinement dependency (default 0.5 [42])	Assumed unless advanced stiffness tests available
Ratcheting	β_μ	–	Deviatoric ratcheting contribution	Cyclic triaxial test
	β_K	–	Volumetric ratcheting contribution	Cyclic triaxial test

We note that the friction angle may be calibrated individually for each yield surface using data from monotonic triaxial tests. Alternatively, the nested surfaces can be constructed by linearly scaling the critical state friction angle φ_{c}. For the n^{th} surface within the set of N nested surfaces, we can thus write:

$$\varphi^{(n)} = \frac{n}{N}\,\varphi_{\text{c}} \tag{65}$$

Hardening in the GCP framework can be defined in two ways. The kinematic hardening modulus $\mathrm{H}_\mu^{\text{kin}}$ for each surface may be calibrated directly from the stress–strain curve of a monotonic triaxial test. Alternatively, when a more compact parameterization is desired, the simplified two-parameter formulation [17] based on h_μ^{kin} and b can be used. Here, b controls the rate at which stiffness decays across the nested surfaces, reproducing the observed reduction in incremental stiffness with loading. The hardening modulus for the n^{th} surface is defined as:

$$H^{(n)} = h\left(1 - \frac{n}{N}\right)^b \tag{66}$$

Here h can be used for either h_μ^{kin}, h_K^{kin}, or h^{iso}. Equation (66) yields a smooth, monotonic sequence $\{H^{(n)}\}_{n=1}^N$ and offers a practical alternative when a simplified but systematic hardening structure is preferred. An initial backstress may be assigned to each surface if required; by default it is taken as zero, producing the configuration shown in Figure 3a.

5.2 Excess pore pressure and cyclic mobility

Cyclic mobility is a liquefaction-related phenomenon that develops under cyclic loading in saturated soils. It is characterized by the progressive accumulation of deformation and excess pore pressure, which causes temporary stiffness degradation and the emergence of continuous residual strains. Numerical difficulties arise near the apex of the yield surface (where $\sigma_1 = \sigma_2 = \sigma_3 = 0$, in Figure 1b), because this point corresponds to a geometric singularity in which surfaces loses smoothness. At this point, $\boldsymbol{n}$ (Eq. (25))

and $\boldsymbol{m}$ (Eq. (10)) become non-differentiable since all deviatoric directions are admissible at $p = q = 0$. The GCP model incorporates specific measures to ensure stable constitutive integration in this region.

Following the approach of Panteghini and Lagioia [40], an apex check is incorporated into the constitutive integration scheme. In their original implementation, a special apex return map is activated when

$$\rho = \|\tilde{\boldsymbol{s}}^{\mathrm{p}}_{\mathrm{dev}}\| = \sqrt{2}J = \sqrt{\frac{2}{3}}\, q = 0 \quad \text{and} \quad \rho^{\mathrm{trial}} = 0 \tag{67}$$

since the deviatoric direction of the normals are not uniquely defined, and only a volumetric flow direction is admissible. Consequently, the deviatoric components of $\boldsymbol{n}$ and $\boldsymbol{m}$ are suppressed and their volumetric parts are used:

$$\boldsymbol{m} = \boldsymbol{m}_{\boldsymbol{v}} = \frac{A_\psi}{3}\,\mathbf{I}, \qquad \boldsymbol{n} = \boldsymbol{n}_{\boldsymbol{v}} = \frac{A_\varphi}{3}\,\mathbf{I} \tag{68}$$

However, the condition in Eq. (67) activates the apex algorithm immediately after isotropic consolidation even under high mean effective stress, which is not physically consistent with our implementation. To avoid this unintended behavior, we modify the apex criterion in the GCP model as:

$$p \leq 0.01\,\mathrm{kPa} \quad \text{and} \quad |q| \leq 0.01\,\mathrm{kPa} \tag{69}$$

This modification enhances robustness near zero effective stress and prevents premature activation of the apex return-mapping. In the low-pressure regime, however, the constitutive equations become highly nonlinear and the Newton-Raphson iterations may experience slow convergence or occasional divergence. To improve stability in these situations, the implementation employs three standard stabilization mechanisms: (i) a backtracking line-search that scales the Newton update to enforce a sufficient decrease in the residual, (ii) diagonal regularization of the Jacobian when it becomes ill-conditioned or nearly singular, and (iii) substepping of the strain increment when convergence cannot be reached within a single iteration. Combined with the use of exact analytical derivatives in the Jacobian, these techniques provide stable and accurate stress integration during cyclic mobility. The resulting behavior is consistent with recent developments in constitutive modeling that emphasize accurately capturing cyclic mobility [56].

To demonstrate this capability, we revisit the test shown in Figures 5c and 5d to simulate cyclic mobility behavior under the same consolidation pressure and deviatoric stress as in the reference study [6]. In the reference study [6], the implicit implementation of the Prevost model fails to converge before reaching $p = 0$ kPa (blue line in Figure 5c), and an explicit scheme is additionally employed to reproduce the characteristic butterfly-shaped stress path. The predictions of the GCP model instead, as illustrated in Figure 6, maintain convergence throughout the cyclic mobility regime and accurately reproduce the butterfly-shaped response, in close agreement with the explicit results reported by Cerfontaine.

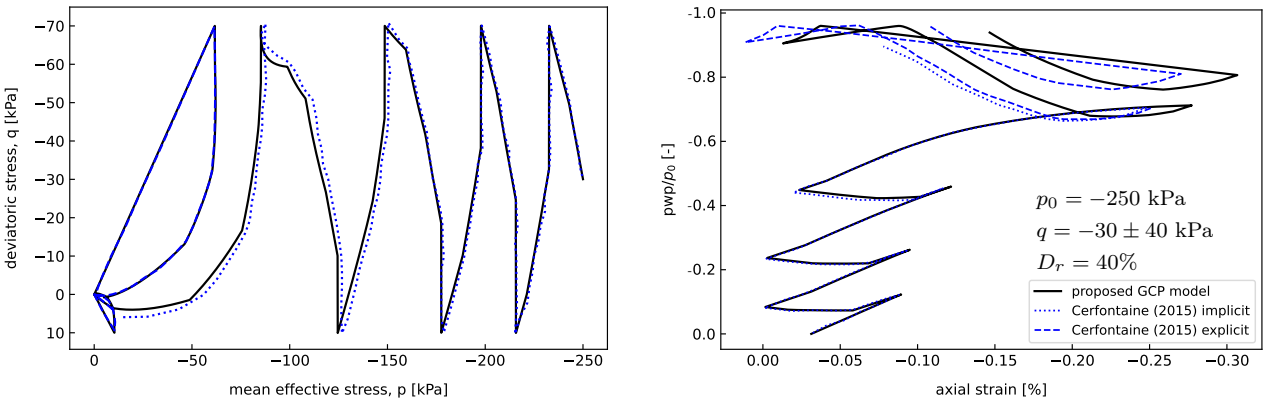

(a) (b)

Figure 6: Cyclic mobility on an undrained cyclic triaxial test simulation at consolidation pressure of $p_0 = -250$ kPa and initial deviatoric stress $q_0 = -30$ kPa. (a) Deviatoric stress q plotted against mean effective stress p and (b) normalized excess pore water pressure plotted against axial strain.

5.3 Stiffness and damping evolution under cyclic loading

Under cyclic loading, the stiffness and damping of sands evolve significantly. For the strain amplitudes considered in this study, the samples exhibit progressive stiffness degradation as cycles accumulate, reflected in the reduction of secant stiffness from one cycle to the next. The damping behavior also evolves during cycling, and its evolution depends on the imposed loading paths.

Figures 7a and 7b present stiffness and damping evolution for the verification example associated with Figures 5a–5b and the cyclic mobility case shown in Figure 6, respectively. In the figures, the start and end points of each loading cycle are marked with "+". Both responses are obtained using the same kinematic hardening formulation and identical kinematic hardening modulus H_{μ}^{kin}. The combination of multisurface plasticity and the pressure-dependent hardening law (Eq. (60)) allows successive yield surfaces to be activated while their position shifts with the mean effective stress, providing a direct mechanism for capturing the evolution of soil state under cyclic loading. The case with stable cyclic response retains a comparatively high stiffness and exhibits narrow hysteresis loops, with energy dissipation remaining low and even decreasing slightly as the response stabilizes. In contrast, the cyclic mobility case develops loops that become progressively flatter and wider, indicating clear stiffness degradation together with a substantial increase in hysteretic damping. This behavior can now be fully observed because the use of the general yield surface concept improves numerical convergence throughout the loading sequence, allowing the complete cyclic mobility loop to be captured.

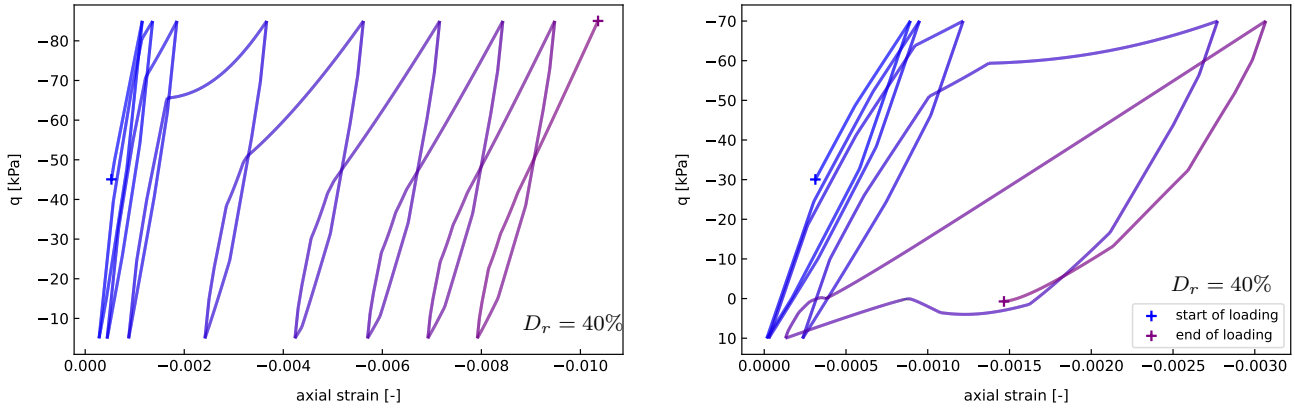

(a) (b)

Figure 7: Evolution of stiffness and damping characteristics with increasing strain amplitude and number of cycles for (a) the case with stable cyclic response, which exhibits high stiffness and low energy dissipation, and (b) the case with cyclic mobility response, which exhibits stiffness degradation and high energy dissipation.

5.4 Lode angle dependency through general yield surface

An important aspect of the formulation is its dependence on the Lode angle, which enables a natural distinction between different deviatoric stress paths. Through this dependence, the model differentiates between triaxial compression and triaxial extension without requiring separate constitutive expressions or parameters, such as M_{c} or M_{e} introduced in classical critical state based models. This yields a more general representation of strength and plastic flow across the entire deviatoric plane and allows the model to capture stress-path effects that cannot be represented using a formulation based solely on the stress invariants p and q. To evaluate the influence of the yield criterion selection, we revisited the verification examples originally conducted with the Drucker–Prager surface (Figures 5a–5b and 6), and repeated them under the same consolidation pressure and deviatoric stress as in the reference study [6] employing

the Matsuoka–Nakai yield surface (Figure 8). Under identical loading conditions, the Matsuoka–Nakai surface, owing to its Lode angle dependency and smaller elastic domain (see Figure 1a), induces a slightly faster reduction in mean effective stress p, with yielding triggered at lower p for the same deviatoric stress.

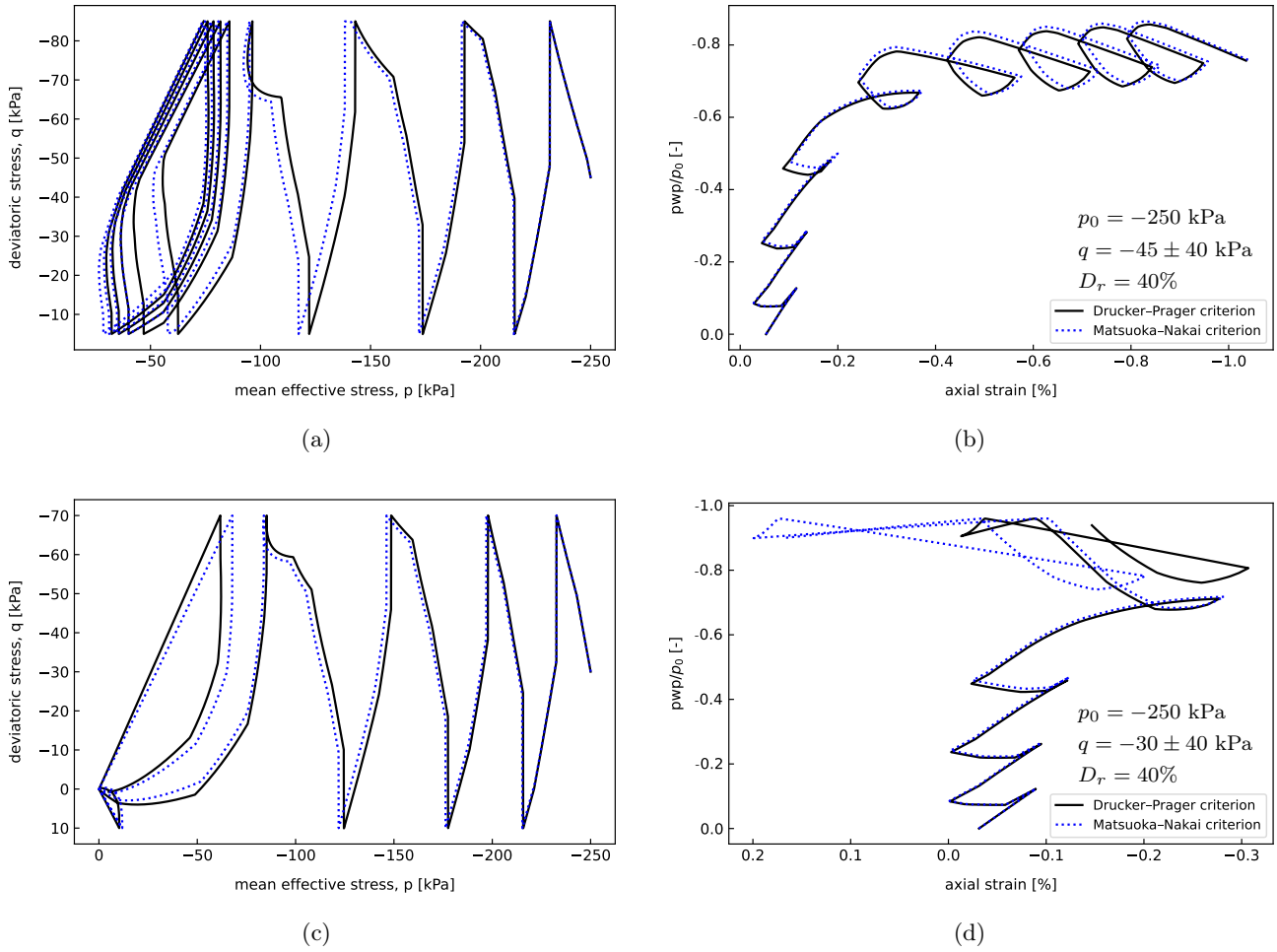

Figure 8: Undrained cyclic triaxial test simulations with the Matsuoka–Nakai type yield criterion with relative density $D_r = 40\%$ and consolidation pressure $p_0 = -250$ kPa. The top row corresponds to initial deviatoric stress $q_0 = -45$ kPa, and the bottom row corresponds to $q_0 = -30$ kPa. (a)–(c) Deviatoric stress q plotted against mean effective stress p and (b)–(d) normalized excess pore water pressure plotted against axial strain.

While this effect is relatively mild under conventional triaxial loading, it becomes more pronounced under non-proportional loading paths such as the direct simple shear (DSS) test, where the intermediate principal stress varies significantly. Therefore, we conducted undrained DSS simulations using the boundary conditions described in Section 3.3. The consolidation pressure was set to $p_0 = -250$ kPa and the initial deviatoric stress to $q_0 = -30$ kPa, consistent with the triaxial tests. The shear stress was varied within $\tau_{xy} = \pm 30$ kPa to capture the nonlinear response. Figure 9 compares the responses using the Drucker–Prager and Matsuoka–Nakai criteria under DSS loading conditions, while retaining the material parameters and the Prevost model formulation adopted from the reference study [6].

Figure 9a presents the resulting p–q stress paths. A faster reduction in p predicted by the Matsuoka–Nakai criterion is clearly observed. Both criteria produce non-smooth trajectories, a well-known feature of DSS simulations due to the highly non-proportional loading and continuous rotation of the principal stress directions. These rotations modify the direction of deviatoric stress evolution, generating local reversals in q even when the imposed loading direction remains unchanged. Figure 9b illustrates

the corresponding shear stress-shear strain responses. Both models exhibit small hysteresis loops during the initial loading stages, which widen progressively as the stress path approaches lower mean effective stresses. The increased loop area reflects strong nonlinear behavior, high energy dissipation, and large accumulated shear strains as the loading state moves toward the apex. Compared to the Drucker–Prager criterion, the Matsuoka–Nakai criterion produces larger strain amplitudes due to its smaller elastic domain resulting from its Lode-angle sensitivity. Differences in the sign of shear strain are attributed to the fixed coordinate system and the initial orientation of the stress state at the onset of cyclic mobility, and are not associated with differences in material response.

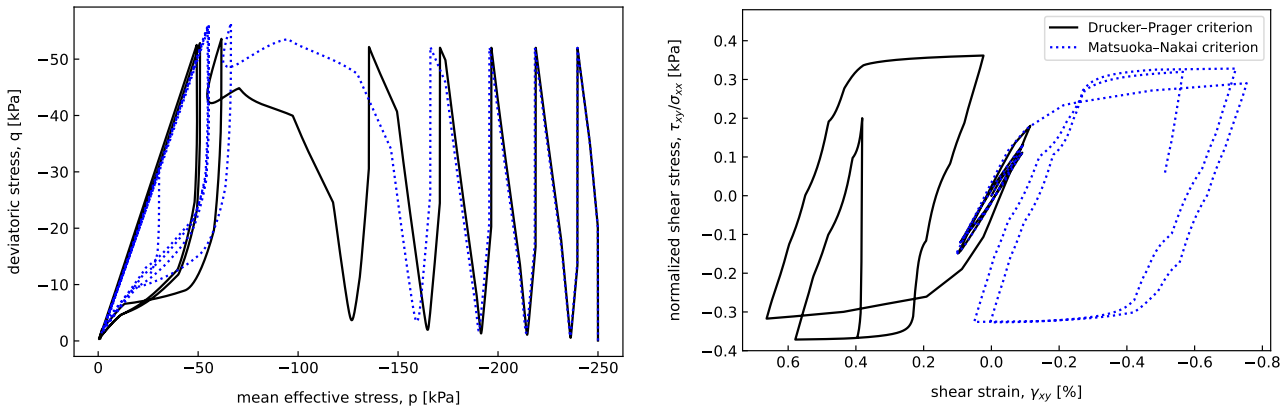

(a) (b)

Figure 9: Undrained DSS test simulation with Matsuoka–Nakai type yield criterion with relative density $D_r = 40\%$ at consolidation pressure of $p_0 = -250$ kPa and deviatoric stress $q_0 = -30$ kPa and shear stress $\tau_{xy} = \pm 30$ kPa. (a) Deviatoric stress q plotted against mean effective stress p and (b) normalized shear stress plotted against shear strain.

5.5 Shakedown response through pressure-dependent combined hardening

The hardening formulation is herein extended beyond classical kinematic hardening by introducing a pressure-dependent isotropic hardening component governed by the evolution equations in Eq. (21). The addition of isotropic hardening provides the model with memory of the loading direction and enhances its ability to capture strain hardening and shakedown behavior under repeated cyclic loading. To ensure physically meaningful behavior near the apex, the isotropic hardening modulus H^{iso} is formulated as a function of the mean effective stress, such that the isotropic hardening naturally diminishes at low pressures. This prevents artificial strengthening as $p \to 0$ and allows the stress state to pass through the apex during cyclic mobility.

To evaluate the influence of pressure-dependent isotropic hardening, we revisit the verification example and compare the response obtained with purely kinematic hardening against that produced by the pressure-dependent combined hardening formulation, using the same consolidation pressure and deviatoric stress as in the reference study [6]. Figure 10 presents the predicted stress–strain response of a sand sample over twenty loading cycles, with the isotropic hardening modulus set to 25% of the kinematic modulus. For reference, the cyclic responses obtained using kinematic hardening alone (Figures 5a–5b and 6) are plotted alongside the new results. The comparison demonstrates that incorporating isotropic hardening leads to a pronounced shakedown response, characterised by reduced cyclic strain accumulation and earlier stabilization of the stress path. This behavior reflects the stabilizing effect of isotropic hardening, which uniformly expands the yield surface while allowing the hardening effect to vanish at low pressures, thereby maintaining realistic behavior near the apex and improving the model's ability to reproduce long-term cyclic response.

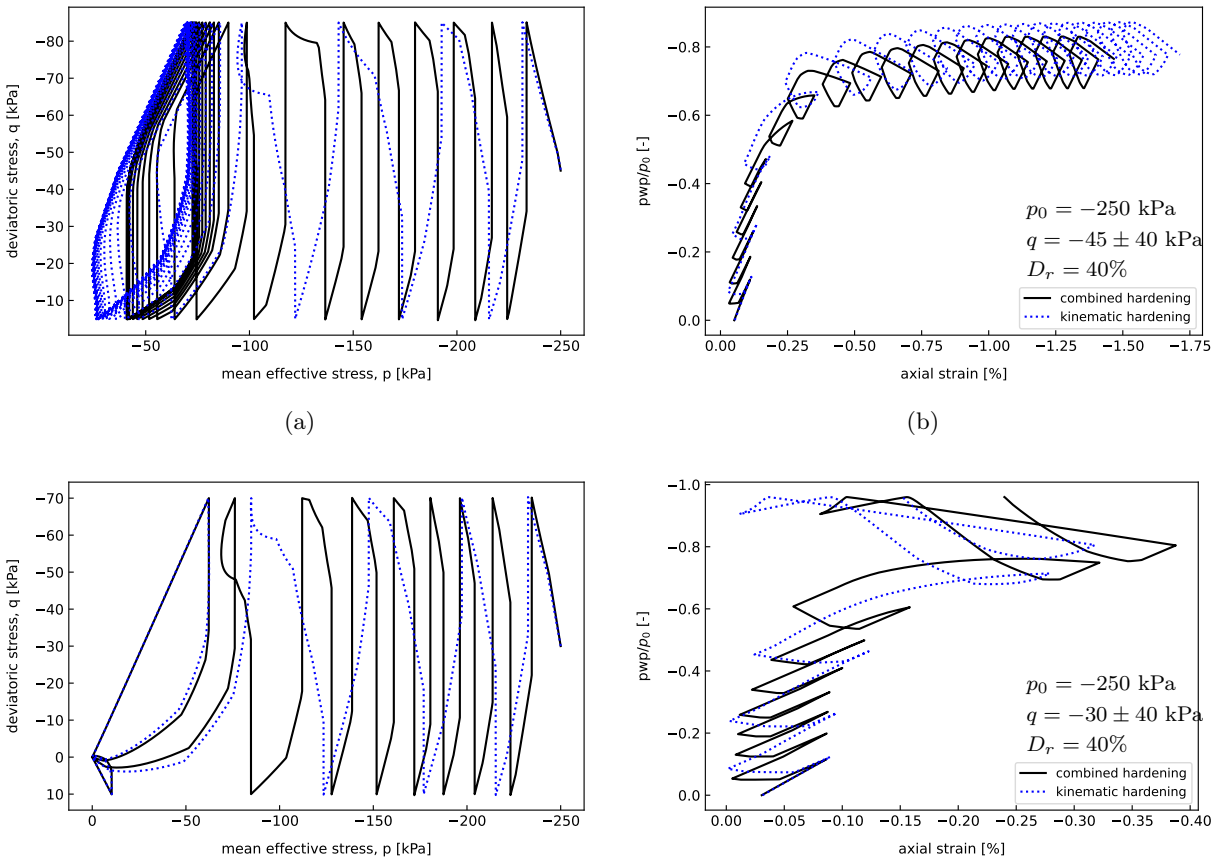

Figure 10: Undrained cyclic triaxial test simulations with a combined hardening feature added on Prevost model, relative density $D_r = 40\%$, and consolidation pressure $p_0 = -250$ kPa. The top row corresponds to initial deviatoric stress $q_0 = -45$ kPa, and the bottom row corresponds to $q_0 = -30$ kPa. (a)–(c) Deviatoric stress q plotted against mean effective stress p and (b)–(d) normalized excess pore water pressure plotted against axial strain.

5.6 State-dependent behavior under monotonic and cyclic loading

The proposed GCP model embeds the principles of critical state soil mechanics (CSSM) through the state parameter Ψ, which provides a unified description of contractive and dilative tendencies. In this formulation, the dilation angle ψ is replaced by a dilation parameter $\bar{\psi}$ that is explicitly linked to the state parameter and combined with phase transformation condition, as defined in Eq. (38). The resulting dilation parameter is then employed within the non-associative flow potential, which is constructed in a thermodynamically consistent manner (Eq. (26)). Because the plastic flow direction follows from a state-dependent potential, the model does not rely on empirical interpolation rules, switching criteria, or ad hoc modifications. As a consequence, the transition from contractive to dilative response is obtained in a clear and continuous manner, and the model naturally evolves toward the critical state under continued shearing, fully consistent with the fundamental principles of critical state soil mechanics. Further, the GCP model incorporates state-dependent kinematic hardening to account for stiffness differences across soil states, together with cyclic-mobility stiffness degradation to represent the progressive loss of stiffness under cyclic loading (Eq. (41)).

The ability of the model to reproduce characteristic sand behavior is examined through selected element-level simulations, validated against laboratory data for Karlsruhe Fine Sand (KFS), a well-documented reference material with an extensive database covering monotonic and cyclic loading un-

der drained and undrained triaxial conditions [53, 52]. The validation is intentionally limited in scope and focuses on verifying the proposed formulation rather than on full parameter calibration. The Matsuoka–Nakai yield surface is adopted in all simulations, and the material parameters used are summarized in Table 5.

Table 5: Material parameters used in the GCP model validation against the KFS database

μ_{ref} [MPa]	K_{ref} [MPa]	λ_{c} [-]	ξ [-]	e_{c0} [-]	n_χ [-]	φ_{c} [°]	M_e [-]	h_μ^{kin} [MPa]	b [-]	n_e [-]	n_h [-]
40	51.6	0.122	0.205	1.103	0.12	33.1	$0.73\,M_c$	100	2.0	8.0	1000

Figure 11 presents a comparison between undrained monotonic triaxial tests from the KFS database and the corresponding GCP model simulations. The selected tests include TMU5 ($e_{\text{init}} = 0.946$), TMU2 ($e_{\text{init}} = 0.814$), and TMU6 ($e_{\text{init}} = 0.728$), covering a wide range of initial densities bounded by $e_{\min} = 0.677$ and $e_{\max} = 1.054$. In all simulations, the initial deviatoric stress was set to $q_0 = 0$ kPa and loading was continued until $q = -400$ kPa. The results demonstrate that the GCP model captures phase transformation behavior and the subsequent approach toward the critical state under undrained monotonic loading. The dependence of the phase transformation stress ratio on the state parameter in Eq. (36) governs the behavior shown in Figure 11a, leading to a clear separation of the phase transformation points in the p–q plane. Figure 11b further shows that, at a fixed consolidation pressure of $p_0 = -200$ kPa, increasing the relative density leads to a higher peak deviatoric stress and a stiffer overall response, whereas lower relative density results in larger axial strains mobilized at the same deviatoric stress, reflecting the softer response of looser sand under undrained conditions. Overall, the simulations exhibit good agreement with the corresponding laboratory responses, reproducing the main features of the stress–strain behavior across the examined range of densities. While a full parameter optimization against the complete experimental database would further improve quantitative agreement, such calibration studies are beyond the scope of the present work, which focuses on the development and verification of the proposed constitutive framework.

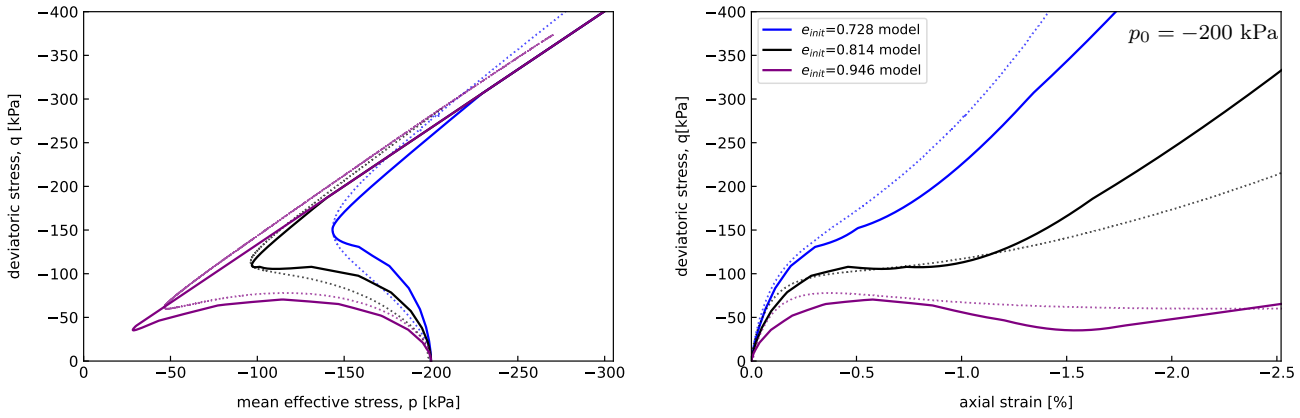

(a) (b)

Figure 11: Validation against undrained monotonic triaxial test from Karlsruhe Fine Sand database for varying initial void ratios at $p_0 = -200$ kPa. Deviatoric stress q plotted against (a) mean effective stress p and (b) axial strain. Solid lines denote GCP model simulations, while dotted lines represent experimental data.

A further parametric study is conducted using the same set of material parameters listed in Table 5 to demonstrate the capabilities of the proposed model. Figure 12 presents undrained monotonic triaxial simulations performed at different consolidation pressures while maintaining a fixed relative density of $D_r = 65\%$. In all cases, the initial deviatoric stress was set to $q_0 = 0$ kPa and loading was continued until

$q = -400$ kPa. The influence of consolidation pressure is illustrated in Figure 12a, where each stress path originates from its respective consolidation state and follows an initially contractive trajectory toward the phase transformation condition. Both the initial stiffness and the peak deviatoric stress increase systematically with consolidation pressure, consistent with the pressure dependence of sand stiffness and strength. This behavior is also reflected in Figure 12b, where the lower-pressure case reaches the phase transformation at smaller axial strains, whereas higher consolidation pressures lead to clearer post-peak softening in the stress–strain response. Correspondingly, the higher-pressure cases develop broader stress paths that remain farther from the origin in the p–q plane during shearing. The strain development in the phase transformation region is directly influenced by the phase transformation condition adopted in this study, as given in Eq. (37). The numerical regularization parameter η_0 controls the rate at which the dilation parameter changes sign as the stress state passes through the zero-dilatancy condition, thereby governing the amount of strain accumulated during this transition. η_0 could be made state dependent, or alternative smooth transition functions could be considered in future studies; however, the emphasis here is on demonstrating the feasibility of embedding critical state soil mechanics within the flow potential through a dilation parameter.

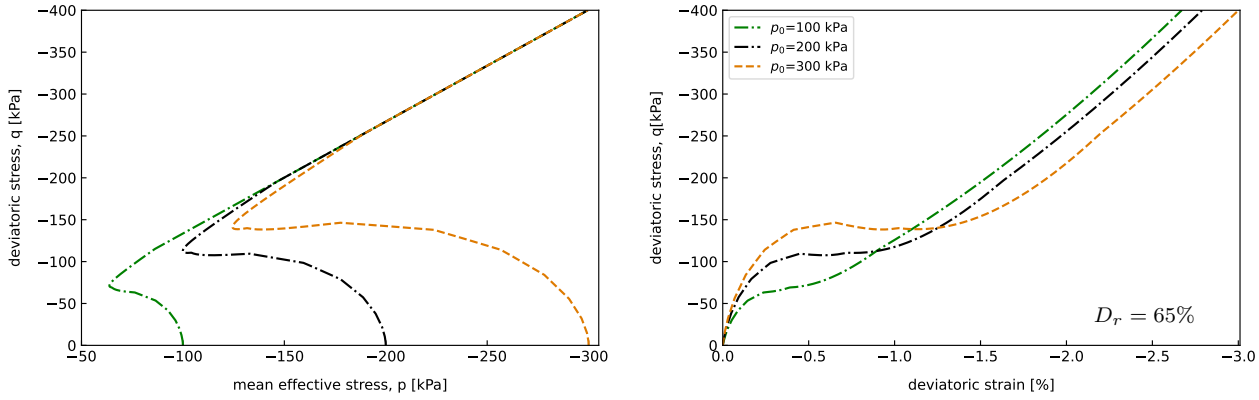

(a) (b)

Figure 12: Undrained monotonic triaxial test simulation with state parameter integration corresponding to varying consolidation pressure at relative density $D_r = 65\%$. (a) Deviatoric stress q plotted against mean effective stress p. (b) Deviatoric stress q plotted against deviatoric strain.

Figure 13 presents undrained cyclic triaxial simulations performed at two initial density conditions. The top row corresponds to the case with a relative density of $D_r = 90\%$, and the bottom row corresponds to the case with a relative density of $D_r = 40\%$, both conducted under a consolidation pressure of $p_0 = -200\,\text{kPa}$. In the figures, the start and end points of each loading cycle are marked with "+". The denser sand exhibits a more stable undrained cyclic response, characterized by slower pore pressure buildup and tighter effective stress loops during cycling. Cyclic mobility is reached after seven loading cycles, as indicated by the stress path approaching the apex of the effective stress space. In contrast, the lower-density material transitions into cyclic mobility at an earlier stage, showing a faster development and enlargement of butterfly-shaped stress loops. In this case, the stress path reaches the cyclic mobility after the first loading cycle, marking an earlier onset. In terms of axial strain response, the looser sand accumulates significantly larger strains after reaching the apex of the stress path, consistent with its more contractive behavior and earlier onset of cyclic mobility. At larger strain levels, the simulations indicate substantially higher axial strain accumulation for the $D_r = 40\%$ case compared with the $D_r = 90\%$ case. This strain accumulation is directly linked to the cyclic-mobility stiffness degradation mechanism employed in the model, as the evolution of the hardening parameter controls the progressive widening of the hysteresis loops and the associated strain growth under repeated loading.

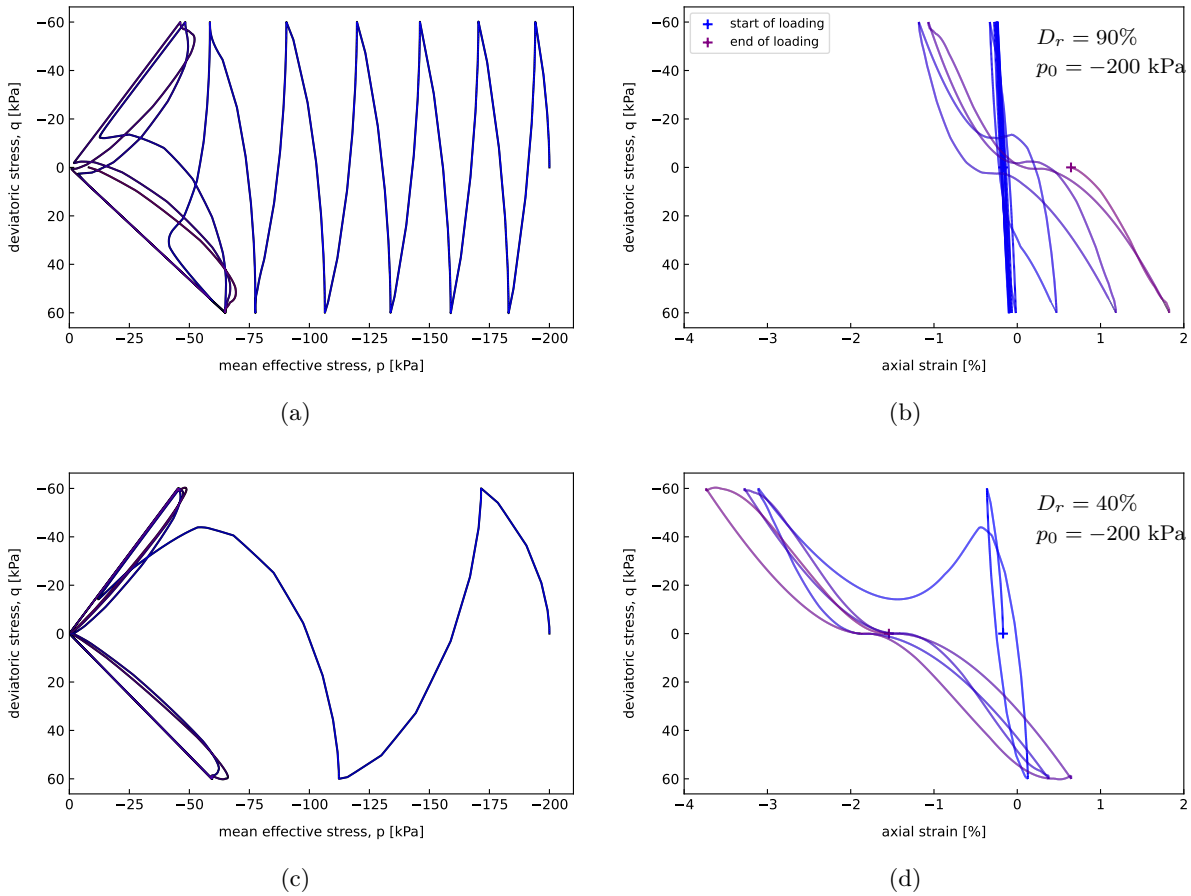

Figure 13: Undrained cyclic triaxial test simulations with state parameter integration at consolidation pressure of $p_0 = -200$ kPa and deviatoric stress $q = 0 \pm 60$ kPa. The top row corresponds to relative density $D_r = 90\%$ and the bottom row corresponds to $D_r = 40\%$. Deviatoric stress q plotted against (a) and (c) mean effective stress p, and (b) and (d) axial strain.

6 Summary and conclusions

This study introduced the Generalized Cyclic Plasticity (GCP) constitutive model for sands, a three-dimensional multisurface plasticity formulation that is thermodynamically consistent and designed to reproduce hysteretic cyclic behavior, satisfy the original Masing rule, and capture the contractive and dilative responses of sands under complex stress paths associated with cyclic loading. Building on Ziegler's two-potential thermodynamic framework, the model incorporates a third potential derived from the generalized principle of maximum dissipation. A dilation parameter that couples the state-controlled peak dilation angle with the phase transformation condition is introduced within this flow potential, enabling a rigorous and physically admissible treatment of non-associative plasticity. Stabilization procedures for complex yield surfaces, particularly Matsuoka–Nakai and Lade–Duncan, were developed to overcome numerical instabilities near the apex and achieve stable constitutive integration across a wide range of stress paths. The model provides a flexible foundation that supports multiple yield criteria, including Matsuoka–Nakai, von Mises, Drucker–Prager, Lade–Duncan, and original and rounded forms of Tresca and Mohr–Coulomb through Lode angle dependent formulation. The GCP model is formulated using a set of soil parameters that correspond directly to measurable features of sand behavior obtained from standard laboratory tests, and this parameter set allows the model to simulate monotonic and cyclic loading over a wide range of applied pressures and density states. The model successfully reproduces cyclic mobility curves by employing exact derivatives and resolves numerical challenges near the apex by activating a spe-

cial apex treatment, a line search procedure, substepping, Jacobian regularization. GCP can incorporate a deviatoric component of kinematic hardening to provide directional memory, an isotropic component to capture cumulative memory effects, and an isotropic hardening mechanism to represent strain hardening and shakedown behavior. The kinematic hardening formulation is extended to account for the soil state and cyclic mobility stiffness degradation. The hardening laws are defined pressure dependent to ensure that cyclic stress paths pass through the origin in mobility plots, and the choice of hardening law is left to the user, providing flexibility. Incorporation of CSSM principles through the state parameter and the phase transformation line enables realistic modelling of state-dependent contraction and dilation across loose and dense conditions without ad hoc adjustments, providing a sound thermodynamic foundation for further developments.

The proposed GCP framework can reproduce a broad range of classical constitutive models for soils, including associative and non-associative Mohr–Coulomb plasticity, the Prevost multisurface model [6], and the variational framework of Ulloa et al. [50]. These formulations are recovered directly through the general yield-surface definition, and the resulting stress–strain and pore-pressure responses remain consistent with their original behavior. This capability mitigates several limitations inherent to the czlassical approaches. Yield surfaces based on second or higher order stress invariants, such as the Drucker–Prager surface in the Prevost model, may become unstable near the apex at low mean stress, while piecewise Mohr–Coulomb or Tresca criteria exhibit integration difficulties due to corners in the deviatoric plane. The linear yield surface representation avoids these issues by ensuring a numerically stable integration by a fully convex general yield function without requiring an additional surcharge on the model. Since the same functional form of yield function is employed to construct the plastic flow potential, non-associativity can be introduced in a thermodynamically consistent manner through the state parameter and its established link to the dilation angle.

This paper has established the conceptual foundations of the GCP model and presented its mathematical formulation in a systematic manner. The focus has been on outlining the governing principles, defining the model equations, and verifying the formulation against reference simulations reported in the literature with particular emphasis on undrained soil behavior. Detailed calibration against laboratory data for specific sands, the extension to drained soil behavior, and applications in large-scale boundary-value analyses involving many loading cycles are beyond the scope of this work and will be investigated in future studies.

REFERENCES

[1] Christelle Nadine Abadie, GT Houlsby, and BW Byrne. A method for calibration of the hyperplastic accelerated ratcheting model (harm). *Computers and Geotechnics*, 112:370–385, 2019.

[2] Larry Armijo. Minimization of functions having lipschitz continuous first partial derivatives. *Pacific Journal of mathematics*, 16(1):1–3, 1966.

[3] Ken Been and Mike G Jefferies. A state parameter for sands. *Géotechnique*, 35(2):99–112, 1985.

[4] MD Bolton. The strength and dilatancy of sands. *Geotechnique*, 36(1):65–78, 1986.

[5] Ross W Boulanger and Katerina Ziotopoulou. Pm4sand (version 3): A sand plasticity model for earthquake engineering applications. *Center for Geotechnical Modeling Report No. UCD/CGM-15/01, Department of Civil and Environmental Engineering, University of California, Davis, Calif*, 2015.

[6] Benjamin Cerfontaine. *The cyclic behaviour of sand, from the Prevost model to offshore geotechnics*. PhD thesis, Universite de Liege, 2015.

[7] Bernard D Coleman and Walter Noll. The thermodynamics of elastic materials with heat conduction and viscosity. In *The foundations of mechanics and thermodynamics: Selected papers*, pages 145–156. Springer, 1974.

[8] Charles-Augustin Coulomb. Essai sur une application des règles des maximis et minimis à quelques problèmes de statique relatifs à l'architecture. In *Mémoires de mathématique et de physique*, volume 7, pages 343–382. De l'Imprimerie Royale, 1776.

[9] Yannis F Dafalias and Majid T Manzari. Simple plasticity sand model accounting for fabric change effects. *Journal of Engineering mechanics*, 130(6):622–634, 2004.

[10] René De Borst, Mike A Crisfield, Joris JC Remmers, and Clemens V Verhoosel. *Nonlinear finite element analysis of solids and structures*. John Wiley & Sons, 2012.

[11] Daniel Charles Drucker and William Prager. Soil mechanics and plastic analysis or limit design. *Quarterly of applied mathematics*, 10(2):157–165, 1952.

[12] J Duque, M Yang, W Fuentes, D Mašín, and M Taiebat. Characteristic limitations of advanced plasticity and hypoplasticity models for cyclic loading of sands. *Acta Geotechnica*, pages 1–23, 2022.

[13] Paul Germain, Pierre Suquet, and Quoc Son Nguyen. Continuum thermodynamics. *ASME Journal of Applied Mechanics*, 50:1010–1020, 1983.

[14] OM Heeres and R De Borst. Implicit integration of non-standard plasticity models. In *Application of Numerical Methods to Geotechnical Problems: Proceedings of the Fourth European Conference on Numerical Methods in Geotechnical Engineering Numge98 udine, Italy October 14–16*, pages 483–492. Springer, 1998.

[15] GT Houlsby. Interpretation of dilation as a kinematic constraint. In D. Kolymbas, editor, *Modern approaches to plasticity*, pages 19–38. Elsevier, 1993.

[16] GT Houlsby, CN Abadie, WJAP Beuckelaers, and BW Byrne. A model for nonlinear hysteretic and ratcheting behaviour. *International Journal of Solids and Structures*, 120:67–80, 2017.

[17] GT Houlsby and Giuseppe Mortara. A continuous hyperplasticity model for sands under cyclic loading. In Th. Triantafyllidis, editor, *Proceedings of the International Conference on Cyclic Behaviour of Soils and Liquefaction Phenomena*, pages 21–26, Bochum, Germany, 2004. Taylor & Francis / A.A. Balkema.

[18] GT Houlsby and IA Richards. Multi-surface and bounding surface models in hyperplasticity. *Computers and Geotechnics*, 156:105143, 2023.

[19] Guy T Houlsby and Alexander M Puzrin. *Principles of hyperplasticity: an approach to plasticity theory based on thermodynamic principles*. Springer Science & Business Media, 2007.

[20] J-C Hujeux. Une loi de comportement pour le chargement cyclique des sols. In *Génie parasismique*, pages 287–302, 1985.

[21] Kenji Ishihara, Fumio Tatsuoka, and Susumu Yasuda. Undrained deformation and liquefaction of sand under cyclic stresses. *Soils and foundations*, 15(1):29–44, 1975.

[22] Nils Janbu. Soil compressibility as determined by oedometer and triaxial tests. In *Proceedings of the European Conference on Soil Mechanics and Foundation Engineering*, volume 1, pages 19–25, Wiesbaden, Germany, 1963.

[23] MG Jefferies. Nor-sand: a simle critical state model for sand. *Géotechnique*, 43(1):91–103, 1993.

[24] Michael Jefferies. On the fundamental nature of the state parameter. *Géotechnique*, 72(12):1082–1091, 2022.

[25] Evangelos Kementzetzidis, Federico Pisanò, and Andrei V Metrikine. A memory-enhanced py model for piles in sand accounting for cyclic ratcheting and gapping effects. *Computers and Geotechnics*, 148:104810, 2022.

[26] Poul V Lade and James M Duncan. Elastoplastic stress-strain theory for cohesionless soil. *Journal of the Geotechnical Engineering Division*, 101(10):1037–1053, 1975.

[27] Rocco Lagioia and Andrea Panteghini. On the existence of a unique class of yield and failure criteria comprising tresca, von mises, drucker–prager, mohr–coulomb, galileo–rankine, matsuoka–nakai and lade–duncan. *Proceedings of the royal society A: mathematical, physical and engineering sciences*, 472(2185):20150713, 2016.

[28] Xiang-Song Li and Y Wang. Linear representation of steady-state line for sand. *Journal of geotechnical and geoenvironmental engineering*, 124(12):1215–1217, 1998.

[29] Hao Yuan Liu, José Antonio Abell, Andrea Diambra, and Federico Pisanò. Modelling the cyclic ratcheting of sands through memory-enhanced bounding surface plasticity. *Géotechnique*, 69(9):783–800, 2019.

[30] W Lode. Versuche über den einfluß der mittleren hauptspannung auf das fließen der metalle eisen, kupfer und nickel. *Zeitschrift für Physik*, 36(11):913–939, 1926.

[31] Majid T Manzari and Yannis F Dafalias. A critical state two-surface plasticity model for sands. *Géotechnique*, 47(2):255–272, 1997.

[32] Jean-Jacques Marigo and Kyrylo Kazymyrenko. A micromechanical inspired model for the coupled to damage elasto-plastic behavior of geomaterials under compression. *Mechanics & Industry*, 20(1):105, 2019.

[33] Hajime Matsuoka and Teruo Nakai. Stress-deformation and strength characteristics of soil under three different principal stresses. In *Proceedings of the Japan Society of Civil Engineers*, volume 1974, pages 59–70. Japan Society of Civil Engineers, 1974.

[34] R v Mises. Mechanik der festen körper im plastisch-deformablen zustand. *Nachrichten von der Gesellschaft der Wissenschaften zu Göttingen, Mathematisch-Physikalische Klasse*, 1913:582–592, 1913.

[35] Otto Mohr. Welche umstände bedingen die elastizitätsgrenze und den bruch eines materials. *Zeitschrift des Vereins Deutscher Ingenieure*, 46(1524-1530):1572–1577, 1900.

[36] Francisco J Montáns and Ronaldo I Borja. Implicit J_2-bounding surface plasticity using prager's translation rule. *International journal for numerical methods in engineering*, 55(10):1129–1166, 2002.

[37] Zi Mroz. On the description of anisotropic workhardening. *Journal of the Mechanics and Physics of Solids*, 15(3):163–175, 1967.

[38] TD Nguyen, JM Fleureau, and A Modaressi. Identification of parameters and validation of hujeux. In *Prediction, Analysis and Design in Geomechanical Applications: Proceedings of the Eleventh International Conference on Computer Methods and Advances in Geomechanics, Torino, Italy, 19-24 June 2005*, volume 3, page 433. Pàtron Editore, 2005.

[39] Andrzej Niemunis, Torsten Wichtmann, and Th Triantafyllidis. A high-cycle accumulation model for sand. *Computers and geotechnics*, 32(4):245–263, 2005.

[40] Andrea Panteghini and Rocco Lagioia. A fully convex reformulation of the original matsuoka–nakai failure criterion and its implicit numerically efficient integration algorithm. *International Journal for Numerical and Analytical Methods in Geomechanics*, 38(6):593–614, 2014.

[41] Jean H Prevost. Two-surface versus multi-surface plasticity theories: A critical assessment. *International Journal for Numerical and Analytical Methods in Geomechanics*, 6(3):323–338, 1982.

[42] Jean H Prevost. A simple plasticity theory for frictional cohesionless soils. *International Journal of Soil Dynamics and Earthquake Engineering*, 4(1):9–17, 1985.

[43] Jean-Hervé Prévost. Mathematical modelling of monotonic and cyclic undrained clay behaviour. *International Journal for Numerical and Analytical Methods in Geomechanics*, 1(2):195–216, 1977.

[44] M. Saberi, L. E. J. Simonin, G. T. Houlsby, and B. W. Byrne. Three dimensional finite element simulation of monopiles for offshore wind turbines using the hysand constitutive model. In *Proceedings of the 5th International Symposium on Frontiers in Offshore Geotechnics (ISFOG 2025)*, pages 1–7, Nantes, France, June 2025. ISSMGE.

[45] Luc Simonin. *Development of an effective stress model for sand under cyclic loading in the hyperplastic framework*. PhD thesis, University of Oxford, 2023.

[46] Luc EJ Simonin, Guy T Houlsby, and Byron W Byrne. Hysand: A new constitutive model for sand under cyclic loading. In *Challenges and Innovations in Geomechanics: Proceedings of the 16th International Conference of IACMAG-Volume 3*, pages 142–149. Springer, 2022.

[47] SE Stallebrass and RN Taylor. The development and evaluation of a constitutive model for the prediction of ground movements in overconsolidated clay. *Géotechnique*, 47(2):235–253, 1997.

[48] Yifei Sun, Torsten Wichtmann, Wojciech Sumelka, and Mojtaba E Kan. Karlsruhe fine sand under monotonic and cyclic loads: Modelling and validation. *Soil Dynamics and Earthquake Engineering*, 133:106119, 2020.

[49] Henri Edouard Tresca. *Mémoire sur l'écoulement des corps solides*. Imprimerie impériale, 1869.

[50] Jacinto Ulloa, Roberto Alessi, Jef Wambacq, Geert Degrande, and Stijn Francois. On the variational modeling of non-associative plasticity. *International Journal of Solids and Structures*, 217:272–296, 2021.

[51] T Wichtmann, W Fuentes, and Th Triantafyllidis. Inspection of three sophisticated constitutive models based on monotonic and cyclic tests on fine sand: Hypoplasticity vs. sanisand vs. isa. *Soil Dynamics and Earthquake Engineering*, 124:172–183, 2019.

[52] Torsten Wichtmann and Theodoros Triantafyllidis. An experimental database for the development, calibration and verification of constitutive models for sand with focus to cyclic loading: part ii—tests with strain cycles and combined loading. *Acta Geotechnica*, 11:763–774, 2016.

[53] Torsten Wichtmann and Theodoros Triantafyllidis. An experimental database for the development, calibration and verification of constitutive models for sand with focus to cyclic loading: part i—tests with monotonic loading and stress cycles. *Acta Geotechnica*, 11:739–761, 2016.

[54] D Muir Wood and K Belkheir. Strain softening and state parameter for sand modelling. *Géotechnique*, 44(2):335–339, 1994.

[55] CP Wroth and RH Bassett. A stress–strain relationship for the shearing behaviour of a sand. *Géotechnique*, 15(1):32–56, 1965.

[56] Ming Yang, Mahdi Taiebat, and Yannis F Dafalias. Sanisand-msf: a sand plasticity model with memory surface and semifluidised state. *Géotechnique*, 72(3):227–246, 2022.

Supporting information

An example code and an animation of the yield surface evolution will be openly available on the KU Leuven webpage titled *Offshore Geotechnics*, at URL: `https://bwk.kuleuven.be/projects/offshoregeotechnics/offshore-geotechnics` (under continuous update).

Funding information

Cyclic soil-structure interaction framework for the foundations of offshore renewable energy structures project, funded by the "KU Leuven Global PhD Partnerships with The University of Melbourne" scheme (GPUM/21/023) and "The University of Melbourne Chancellery Strategic International Research Collaboration" funds.

Appendix

A Influence of the state parameter on the dilation angle

Figure 14 illustrates the relationship between the state parameter Ψ and the peak dilation angle ψ_{peak} as defined by Eq. (35). The material constant χ sets the slope of this Ψ–ψ_{peak} relation, linking the state parameter to the resulting dilation angle. Since Ψ can take both negative and positive values, the formulation consistently represents both contractive and dilative behavior.

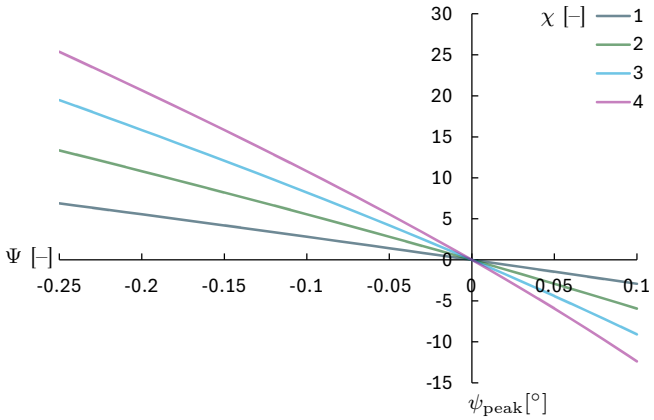

Figure 14: Effect of the material constant χ on the relationship between state parameter Ψ and peak dilation angle ψ_{peak}. Higher χ values predict larger dilation angles at a given Ψ.

B Derivatives of the yield function employed in Jacobian

The Jacobian matrix elements $\frac{\partial f}{\partial \boldsymbol{\sigma}}$ and $\frac{\partial f}{\partial \boldsymbol{\alpha}}$ appearing in Eq. (46) require careful evaluation, particularly when the backstress depends on the mean effective pressure. This dependence introduces additional terms through the chain rule.

Backstress independent of mean pressure When the backstress is independent of the mean effective pressure (see Eq. (19)), the generalized stress is defined as:

$$\boldsymbol{s}^{\text{p}} = \boldsymbol{\sigma} - \boldsymbol{\alpha}$$

Thus, the partial derivatives are:

$$\frac{\partial \boldsymbol{s}^{\text{p}}}{\partial \boldsymbol{\sigma}} = \mathbf{I}, \qquad \frac{\partial \boldsymbol{s}^{\text{p}}}{\partial \boldsymbol{\alpha}} = -\mathbf{I}$$

Applying the chain rule yields:

$$\frac{\partial f}{\partial \boldsymbol{\sigma}} = \frac{\partial f}{\partial \boldsymbol{s}^{\text{p}}} \frac{\partial \boldsymbol{s}^{\text{p}}}{\partial \boldsymbol{\sigma}}, \qquad \frac{\partial f}{\partial \boldsymbol{\alpha}} = \frac{\partial f}{\partial \boldsymbol{s}^{\text{p}}} \frac{\partial \boldsymbol{s}^{\text{p}}}{\partial \boldsymbol{\alpha}}$$

If $\dfrac{\partial f}{\partial \boldsymbol{s}^{\text{p}}} = \boldsymbol{n}$ (see Eq. (25)), then

$$\frac{\partial \mathbf{r}_{\boldsymbol{\sigma}}}{\partial \boldsymbol{\sigma}} = \boldsymbol{n}, \qquad \frac{\partial \mathbf{r}_{\boldsymbol{\sigma}}}{\partial \boldsymbol{\alpha}} = -\boldsymbol{n} \tag{70}$$

Backstress dependent on mean pressure When the backstress depends on the mean effective pressure (see Eq. (60)), the structure of the derivatives changes because $\boldsymbol{s}^{\mathrm{p}}$ now includes the contribution of p to $\boldsymbol{\alpha}$. For an incremental update,

$$\boldsymbol{s}^{\mathrm{p}} = \boldsymbol{\sigma} - \mathbf{H}^{\mathrm{kin}} : (\boldsymbol{\varepsilon}^{\mathrm{p}})^{\mathrm{trial}} - p\,\dot{\boldsymbol{\alpha}}$$

The resulting partial derivatives are:

$$\frac{\partial \boldsymbol{s}^{\mathrm{p}}}{\partial \boldsymbol{\sigma}} = \mathbf{I} - \dot{\boldsymbol{\alpha}} \otimes \frac{\mathbf{1}}{3}, \qquad \frac{\partial \boldsymbol{s}^{\mathrm{p}}}{\partial \boldsymbol{\alpha}} = -p\,\mathbf{I}$$

Here, $\mathbf{1} = \{1,\,1,\,1,\,0,\,0,\,0\}^{\mathrm{T}}$ denotes the volumetric direction vector in Voigt notation.
Substituting these expressions into the chain rule updates Eq. (70) to:

$$\frac{\partial \mathbf{r}_{\boldsymbol{\sigma}}}{\partial \boldsymbol{\sigma}} = \boldsymbol{n}\frac{\partial \boldsymbol{s}^{\mathrm{p}}}{\partial \boldsymbol{\sigma}}, \qquad \frac{\partial \mathbf{r}_{\boldsymbol{\sigma}}}{\partial \boldsymbol{\alpha}} = \boldsymbol{n}\frac{\partial \boldsymbol{s}^{\mathrm{p}}}{\partial \boldsymbol{\alpha}} \tag{71}$$

C Pseudo-algorithm for triaxial test simulations

Algorithm 1 Return mapping algorithm

Require: Initial stress $\boldsymbol{\sigma}$, strain increment $\Delta\boldsymbol{\varepsilon}$, tolerance tol, max iterations
Ensure: Updated stress $\boldsymbol{\sigma}$, plastic strain increment $\Delta\boldsymbol{\varepsilon}^{p}$

```
while min(q0 ± q_cyc) < q < max(q0 ± q_cyc) do
    σ^trial ← σ + C · Δε                                   ▷ compute elastic (trial) stress
    if all f(σ^trial, α^n, h^n) ≤ 0 then
        σ ← σ^trial                                        ▷ elastic loading
    else                                                   ▷ plastic loading
        N_act ← sum(f > 0)                                 ▷ number of active yield surfaces
        Δλ^active ← zeros(N_act, 1)
        x ← {σ^trial, α^active, h^active, Δλ^active}^T     ▷ initialize x with active surfaces
        for iteration ← 1 to max_iteration do
            [σ, α, h, Δλ] ← x
            if p^(n) ≥ 0 then                              ▷ return mapping to the apex
                n^(n), m^(n), (∂m/∂s^p)^(n) ← return_map(s^p(n), "apex")
            else                                           ▷ to the smooth surface
                n^(n), m^(n), (∂m/∂s^p)^(n) ← return_map(s^p(n), "smooth")
            end if
            r ← {r_σ, r_α, r_h, r_f}^T                     ▷ compute residual
            if ||r|| < tol then                            ▷ check the normalized error
                break
            else
                compute derivatives and construct J
                Δx ← −J^−1 r                               ▷ compute the variable updates
                x ← x + ω Δx                               ▷ scale Δx with line search parameter and update x
            end if
        end for
    end if
    Δε^p ← Δλ m
end while
```